NorthWest Research Associates
P.O. Box 3027 • Bellevue, WA 98009-3027

NWRA-CR-95-R142 14 August 1995

Laboratory Studies of Gravity Wave, Mean Flow Interactions

Final Technical Report

for Contract F49620-92-C-0005

by
Donald P. Delisi

for
Maj. James Kroll, Program Manager, AFOSR/NL
Air Force Office of Scientific Research
Bolling AFB, DC 20332-0001

300-120th Ave. N.E. • Suite 220, Building 7 • Bellevue, WA 98005 • (206) 453-8141 • FAX (206) 646-9123

NWRA-CR-95-R142

14 August 1995

Laboratory Studies of Gravity Wave, Mean Flow Interactions

Final Technical Report

for Contract F49620-92-C-0005

by
Donald P. Delisi

for
Maj. James Kroll, Program Manager, AFOSR/NL
Air Force Office of Scientific Research
Bolling AFB, DC 20332-0001

REPORT DOCUMENTATION PAGE

Form Approved
OMB No. 0704-0188

1. AGENCY USE ONLY *(Leave blank)*	2. REPORT DATE	3. REPORT TYPE AND DATES COVERED
	14 August 1995	Final Technical Report, 15 Nov 1991 - 14 Nov 1994

4. TITLE AND SUBTITLE
Laboratory Studies of Gravity Wave, Mean Flow Interactions

5. FUNDING NUMBERS
F49620-92-C-0005

6. AUTHOR(S)
Donald P. Delisi

7. PERFORMING ORGANIZATION NAME(S) AND ADDRESS(ES)
Northwest Research Associates, Inc.
300 120th Ave NE, Bldg 7, Ste 220
P.O. Box 3027
Bellevue, WA 98009-3027

8. PERFORMING ORGANIZATION REPORT NUMBER
NWRA-CR-95-R142

9. SPONSORING / MONITORING AGENCY NAME(S) AND ADDRESS(ES)
USAF, AFMC
Air Force Office of Scientific Research
110 Duncan Avenue, Suite B115
Bolling AFB DC 20332-0001

10. SPONSORING / MONITORING AGENCY REPORT NUMBER

11. SUPPLEMENTARY NOTES

12a. DISTRIBUTION / AVAILABILITY STATEMENT
Unlimited

12b. DISTRIBUTION CODE

13. ABSTRACT (Maximun 200 words)

Laboratory observations of gravity wave, critical layer experiments are presented. In the experiments, a stratified shear flow is generated, and internal gravity waves are allowed to propagate into the flow. The waves propagate up to, but no farther than, their critical layer, the depth where the mean flow equals the horizontal phase speed of the wave. Results are presented with one and two internal waves propagating into the flow. Measurements include mean density and velocity profiles, instantaneous density and velocity profiles, shadowgraph observations, Digital Particle Imaging Velocimetry, and Richardson number estimates. The results show that early wavebreaking is Kelvin-Helmholtz. Later wavebreaking is characterized by internal mixing regions. With the two-wave forcing, the observed late-time turbulence is correlated with the internal wave amplitude.

14. SUBJECT TERMS
Critical layer; Internal waves; Stratified shear flows; Wave, mean flow interactions.

15. NUMBER OF PAGES
56

16. PRICE CODE

17. SECURITY CLASSIFICATION OF REPORT	18. SECURITY CLASSIFICATION OF THIS PAGE	19. SECURITY CLASSIFICATION OF ABSTRACT	20. LIMITATION OF ABSTRACT
Unclassified	Unclassified	Unclassified	

Table of Contents

List of Table and Figures

1. Introduction

This report is the Final Technical Report for contract number F49620-92-C-0005 from the Air Force Office of Scientific Research to Northwest Research Associates, Inc. The research area is laboratory studies of gravity wave, mean flow interactions. The period of performance covered by this report is 15 November 1991 to 14 November 1994.

The next section, Section 2, contains a review of gravity wave, mean flow interactions, with an emphasis on previous laboratory experiments. In Section 3, we discuss our experimental facility; in Section 4 we present our results. A summary and comments are in Section 5. A reprint from *Applied Mechanics Review* is included in the Appendix.

2. Background

Atmospheric gravity waves have a large range of length and time scales. They are important in atmospheric circulation for transporting momentum and for generating turbulence, thereby producing mixing. One mechanism for the breakdown of gravity waves into turbulence and mixing occurs as a wave approaches its critical level, where the mean flow equals the horizontal phase speed of the wave (Booker and Bretherton, 1967).

It is important to understand how gravity waves propagate and dissipate in the atmosphere to be able to predict atmospheric circulation. The interactions and couplings between large-scale and small-scale atmospheric phenomena are not well understood, and this lack of understanding explains, in part, our inability to predict atmospheric conditions globally or locally very far in advance. For example, studies have shown that terrain has a significant effect on the variance in the troposphere and the stratosphere (Nastrom et al, 1987) and that breaking gravity waves (such as might occur in gravity wave, critical layer interactions) are important in the large-scale flow in the troposphere and lower stratosphere. Hence, local topography generates mesoscale gravity waves, and these waves are important globally as well as locally.

Linear theory for the interaction of a gravity wave with a critical layer was first developed by Bretherton (1966) and Booker and Bretherton (1967). Subsequent theoretical and numerical research has been performed by Benney and Bergeron (1969), Maslowe (1973, 1977), Grimshaw (1975), Fritts (1978, 1979, 1982), Brown and Stewartson (1980), Dunkerton (1980, 1981, 1982), Lindzen (1981), Dunkerton and Fritts (1984), Dunkerton and Robins (1992), and many others. For reviews, see Fritts (1984), Maslowe (1986), and Andrews et al (1987).

Observationally, it has been difficult to locate and observe gravity wave, critical layer interactions in the atmosphere. To help understand this phenomenon, several gravity wave, critical layer experiments have been performed under controlled, laboratory conditions. Using monochromatic waves, laboratory experiments have been reported by Thorpe (1973, 1981), Koop (1981), and Koop and McGee (1986). In these experiments, the gravity waves were generated by a corrugated bottom floor. The interaction of a broadband gravity wave source with shear was also reported in Bretherton et al (1967) and, cited above, Koop (1981) and Koop and McGee (1986). In these experiments, a triangular-shaped obstacle or a cylinder generated the broadband wave signal. In all these laboratory experiments:

(a) the results were primarily qualitative and were presented as flow visualization results or as point sensor temporal plots,

(b) due to limitations of the experimental facilities, only short-time (several minutes or less) gravity wave, critical layer interactions could be studied, and

(c) the horizontal wavelengths of the forced gravity waves were small, generally less than 15-25 cm, and, hence, viscosity may have been important in the overturning regions, where typical length scales are a fraction of the horizontal wavelength of the incoming wave.

Our previously reported laboratory study of gravity wave, critical layer interactions with monochromatic waves (Delisi and Dunkerton, 1989) differed from the above studies in three ways:

(a) we were the first to report quantitative measurements of the mean flow modifications due to the interactions,

(b) long-time interactions were reported, with observed interaction times of over an hour, and

(c) the forced gravity waves had a horizontal wavelength of 240 cm, an order of magnitude larger than previous studies.

In this study, we will expand on the results reported in Delisi and Dunkerton (1989) by further examining single wave forcing and by examining gravity wave, critical layer interactions using two monochromatic waves for the wave forcing. Reduced funding prevented examination of gravity wave, critical layer interactions using a compact, broadband wave source, as originally proposed.

3. Review of the Experimental Facility

The experimental facility consists of an annular wave tank, computers to run the experiment and to acquire the probe measurements, power supplies and motor drivers to drive the forcing wave, and flow measurement and visualization equipment. To perform an experiment, the tank was filled with salt-stratified water, a lid was rotated on the water surface to generate a shear, and gravity waves were generated on the bottom floor of the tank by moving the floor vertically up and down. The gravity waves generated at the floor propagated up into the tank, reached a critical level where the current speed equaled the phase speed of the wave, and interacted with the mean flow. The interaction was measured with probes and observed with flow visualization.

The tank consists of two concentric acrylic walls, 1.8 and 1.2 m in diameter, and 40 cm high (Figure 1). The acrylic is attached to, and supported by, circular aluminum frames. The frames extend below the acrylic walls to support the floor actuation equipment. The floor membrane is made out of resilient, rubberized material used in scuba diving wetsuits. Under the

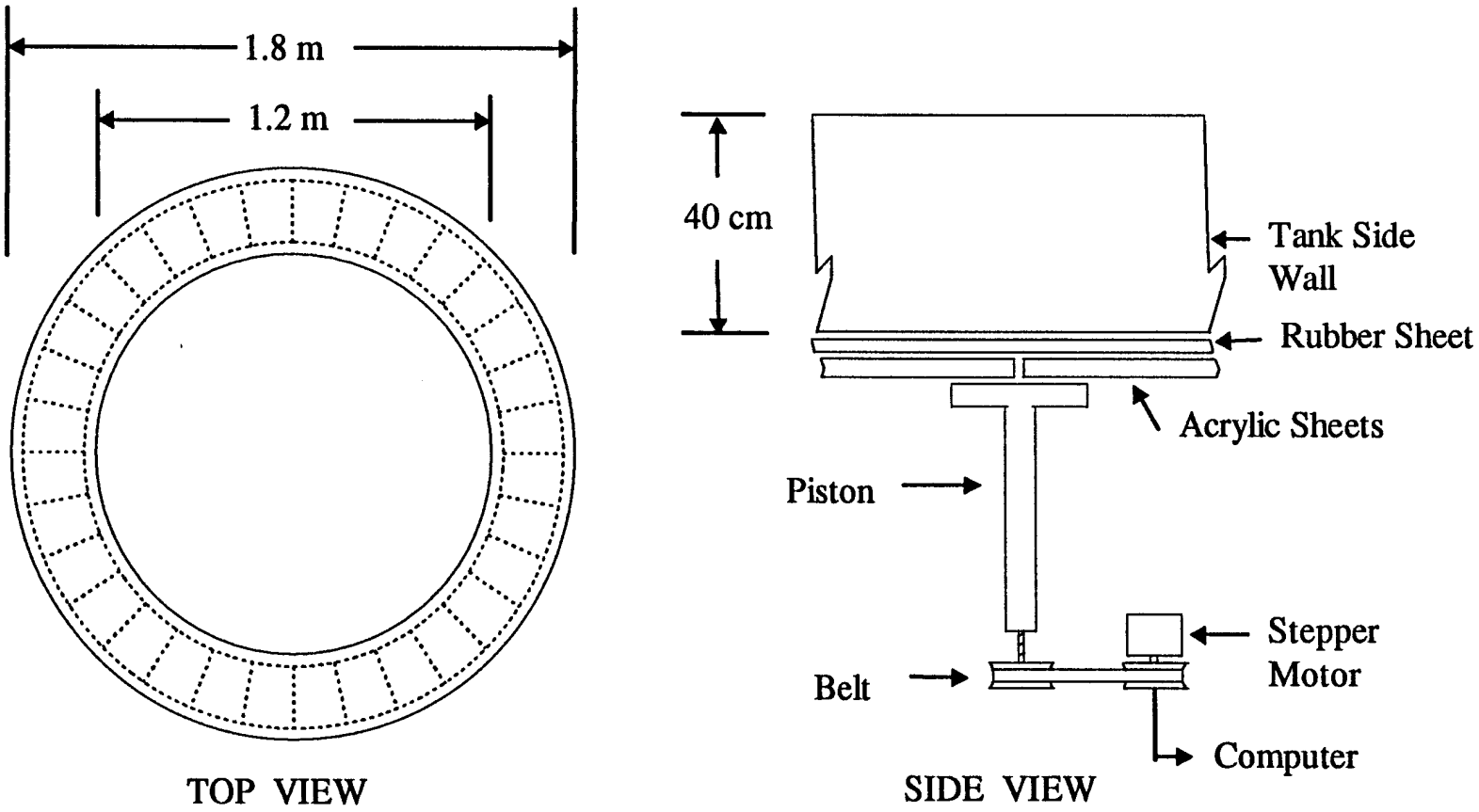

Figure 1. Schematic drawing of the experimental facility. One of 32 piston assemblies is shown in the side view.

membrane are 32 pie-shaped pieces of acrylic, joined end to end to form a continuous ring. At the junction between each floor piece is a tee-shaped aluminum piston. The top of the tee runs along and supports the junction between adjacent pie-pieces, and the vertical portion extends downward. At the bottom of the tee is a ballnut. A ballshaft threads into the ballnut, and extends down to and through a flange bearing. By turning the ballshaft, the ballnut, the tee, and the associated section of the floor move up and down.

The ballshaft is coupled to a stepper motor via a drive belt. Each stepper motor has a stepper motor driver that receives its signals from a computer. The motors are powered by two 3-phase, 3000-watt DC power supplies. For fast response, the motors are driven through resistors that are 10 times the internal resistance of the motors.

The tank has a "lid" that is an acrylic ring of the same nominal dimension as the floor of the tank. In shape it is flat like a large "O," but it is trimmed for a loose fit into the tank. The inner and outer perimeters have 5 cm high walls, so the lid can float on the water in the tank. The outer wall has a groove for a long rubber drive cord. Four brass spindles are located around the perimeter of the main tank, one being powered. The drive cord is passed around the lid, and pulled away from the lid to go outside the spindles. This centers the lid in the tank. The powered spindle makes the lid rotate; this rotation generates the shear flow.

Neutrally buoyant particles are placed in the flow prior to the tank being filled. The particles are made of S6F Pliolite, a styrene-butadiene polymer. The particles are illuminated in a thin, vertical sheet near the tank center line during an experiment. Time exposures of the particles by a 35-mm camera on the side of the tank yield streak photographs of the particle motions. These steak photographs yield vertical profiles of instantaneous particle velocity. The average of these vertical profiles over one wave period yields the mean velocity (Delisi and Dunkerton, 1989).

The particles are also used to obtain two-dimensional velocity field measurements using Digital Particle Imaging Velocimetry (DPIV; Willert and Gharib, 1991). The DPIV system consists of a Spectra-Physics 5-watt Argon laser, a shutter and timer, and processing software. DPIV measurements were made to correlate shadowgraph measurements with velocity data in overturning regions and to estimate vorticity over a complete wave cycle. These results are presented in Section 4.

A Seabird Electronics Model SBE-7 microstructure conductivity probe extends into the tank from the side, making a right angle near the tank center line. The probe shaft on the outside of the tank is fastened to an arm. Moving the arm causes the probe shaft to rotate, moving the probe tip up and down in the tank. The arm is driven by a crank and pushrod connected to a variable speed gearmotor. The gearmotor also drives a position encoder that generates 512 square waves and one index pulse for each cycle of the conductivity probe. These square waves and index pulses are stored by the data acquisition computer and are used in later analysis to determine density vs. probe depth.

4. Results

4.1 General results

To perform an experiment, we filled the tank with a stratified salt water solution, rotated the lid at the water surface to create a shear profile, then propagated one or two waves on the bottom floor of the tank by moving the floor vertically with the stepper motors. Measurements consisted of instantaneous density data from the oscillating conductivity probe, bottom floor position data, particle streak photographs (used to obtain mean and instantaneous velocity profiles), 35-mm and video pictures of shadowgraph flow visualization, and, in some instances, DPIV data. Table 1 gives the relevant information for the runs discussed in this report.

Table 1. Relevant data for the runs discussed in this report. All waves had wavenumber = 2.

Run	N_{top} (sec^{-1})	N_{bottom} (sec^{-1})	Phase Speed (cm/sec)	Peak-to-Peak Amplitude (cm)	Phase Speed (cm/sec)	Peak-to-Peak Amplitude (cm)
38	1.56	0.92	3.5	4.0	-	-
111	1.54	0.99	4.5	4.0	-	-
141	1.57	1.00	4.5	3.0	3.5	3.0
151	1.62	1.02	4.5	3.0	3.5	3.0
161	1.65	1.03	4.5	4.0	-	-
171	1.61	1.02	4.5	4.0	3.5	1.0
191	1.58	1.03	4.5	4.0	3.5	2.0
211	1.44	0.85	4.5	4.0	-	-
221	1.44	0.85	4.5	4.0	-	-

We used two, linearly stratified density layers in these experiments. Data from 3 runs are shown in Figure 2. In these runs, the density profile was nominally identical, with a highly stratified region at the top of the tank and a lighter stratification in the bottom of the tank. In Figure 2, the data are shown by the symbols, and the straight lines are shown for comparison to linearity. The average Brunt-Vaisala frequency, N, for the top layer is 1.63 sec^{-1} where

$$N = \left(\frac{-g}{\bar{\rho}} \frac{\partial \rho}{\partial z}\right)^{\frac{1}{2}} \qquad (1)$$

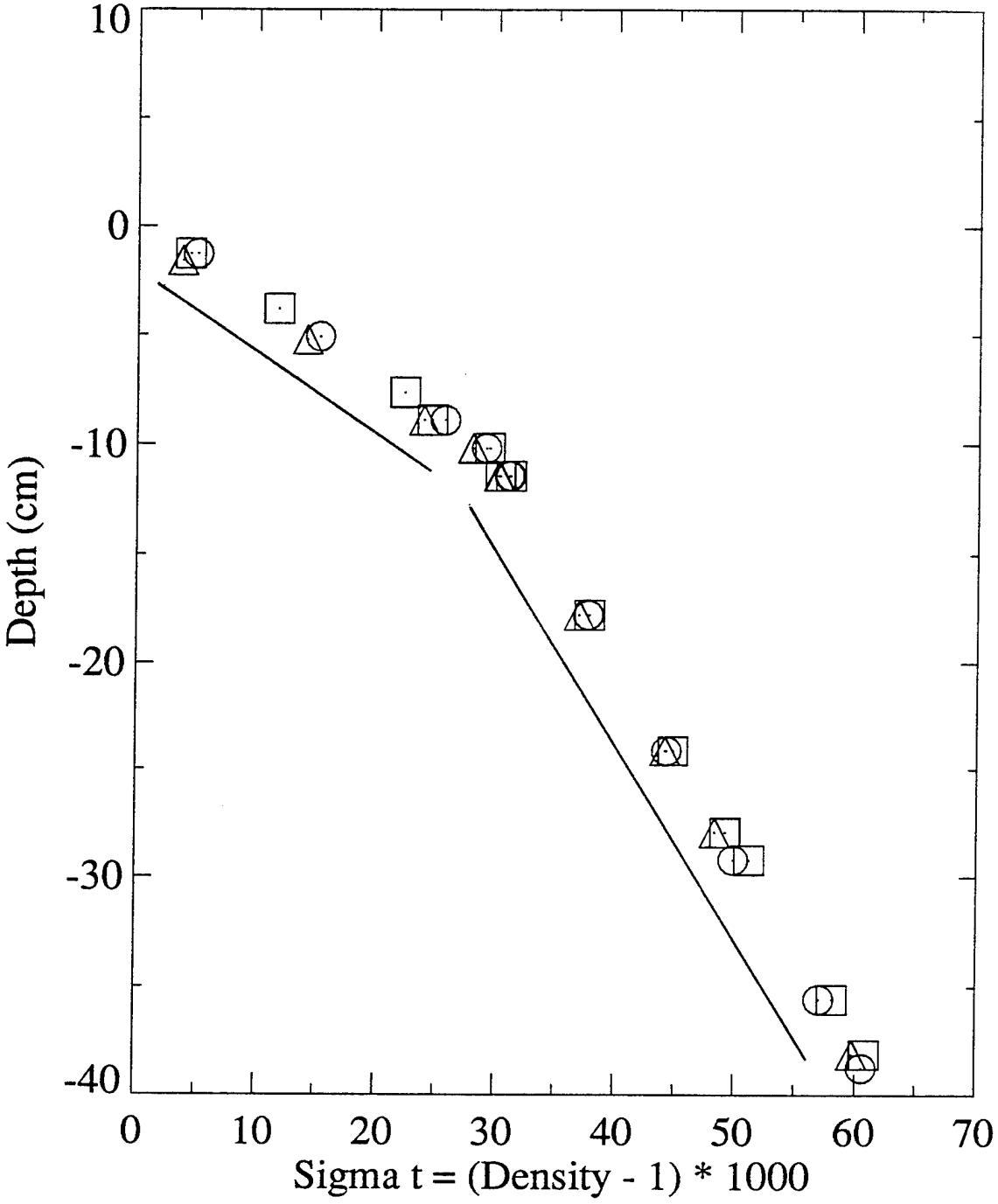

Figure 2. Nominally identical density profiles from three runs. Circles are from Run 151, squares are from Run 161, and triangles are from Run 171. Straight lines are shown for comparison to linearity.

where g is the acceleration due to gravity, $\bar{\rho}$ is mean density, ρ is density, and z is the vertical coordinate. The value of N in the upper layer was chosen to minimize the depth of the mixed layer generated by the rotation of the lid. Because the mixed layer growth is inhibited by a stronger stratification, the value of N in the upper layer was made as large as practically possible. The value of N in the lower layer is chosen from considerations of the dissipation scale height, d, given by

$$d \sim \frac{k\hat{c}^4}{\nu N^3} \qquad (2)$$

where k is the zonal wavenumber, $\hat{c} = c - \bar{U}$, c is the phase speed of the forced wave at the bottom floor, $\bar{U}$ is the mean flow speed, and ν is the kinematic viscosity (Plumb and McEwan, 1978). To minimize gravity wave dissipation and to maximize the wave energy reaching a given vertical level, we want d to be as large as possible. For this reason, we use a weaker stratification, hence, a lower value of N, at the bottom of the tank than at the top of the tank. In Figure 2, the average value of N in the lower part of the tank is 1.02 sec^{-1}. Figure 2 also shows that the stratifications are nearly linear in both the top and the bottom of the tank and that the values of N from run to run are reproducible to within a few percent.

The rotating lid was used to generate the mean shear in the tank. The lid was started from rest and brought to full speed in 60 minutes. For these experiments, full speed of the lid was 1 revolution in approximately 31 sec. Figure 3 shows the evolution of the velocity profile. The times given are in minutes before the start of the experiment (the start of the experiment is at T = 0). For this run, T = - 45 minutes is the time the lid reached full speed. Figure 3 shows that the velocity profile reached near-equilibrium at a time of T = - 15 minutes, which was 30 minutes after the lid reached full speed.

The typical depth of the critical layer was around 11 cm below the surface for a wave with a phase speed of 4.5 cm/sec. The typical depth of the critical layer for a wave with a 3.5 cm/sec phase speed was around 1-2 cm deeper.

In all experiments, the results can be separated into two parts. In the early part of an experiment (t < ~ 13 minutes), the turbulence was due to overturning Kelvin-Helmholtz billows. For later times, the turbulence was due to the internal mixing regions discussed in Delisi and Dunkerton (1989 and 1994).

Figure 4 shows a series of shadowgraph visualizations for Run 171 from times of 9 minutes 18 seconds after the start of the bottom floor (9:18) to 9 minutes 25 seconds after the start of the bottom floor (9:25). These visualizations are enhanced digital images of the video of the shadowgraph. The sequence displayed in Figure 4 shows the growth and decay of a series of Kelvin-Helmholtz (K-H) billows. Each picture in this sequence shows a side view of the tank. A clock is shown in the center of the bottom of each picture. The digital clock shows the time in minutes and seconds after the start of the bottom floor; the analog clock shows time of day. Vertical scales are shown on the left and right edges; the scales are in inches below the water surface. A bottom floor indicator is shown in the bottom half of the right-hand edge. This indicator is a

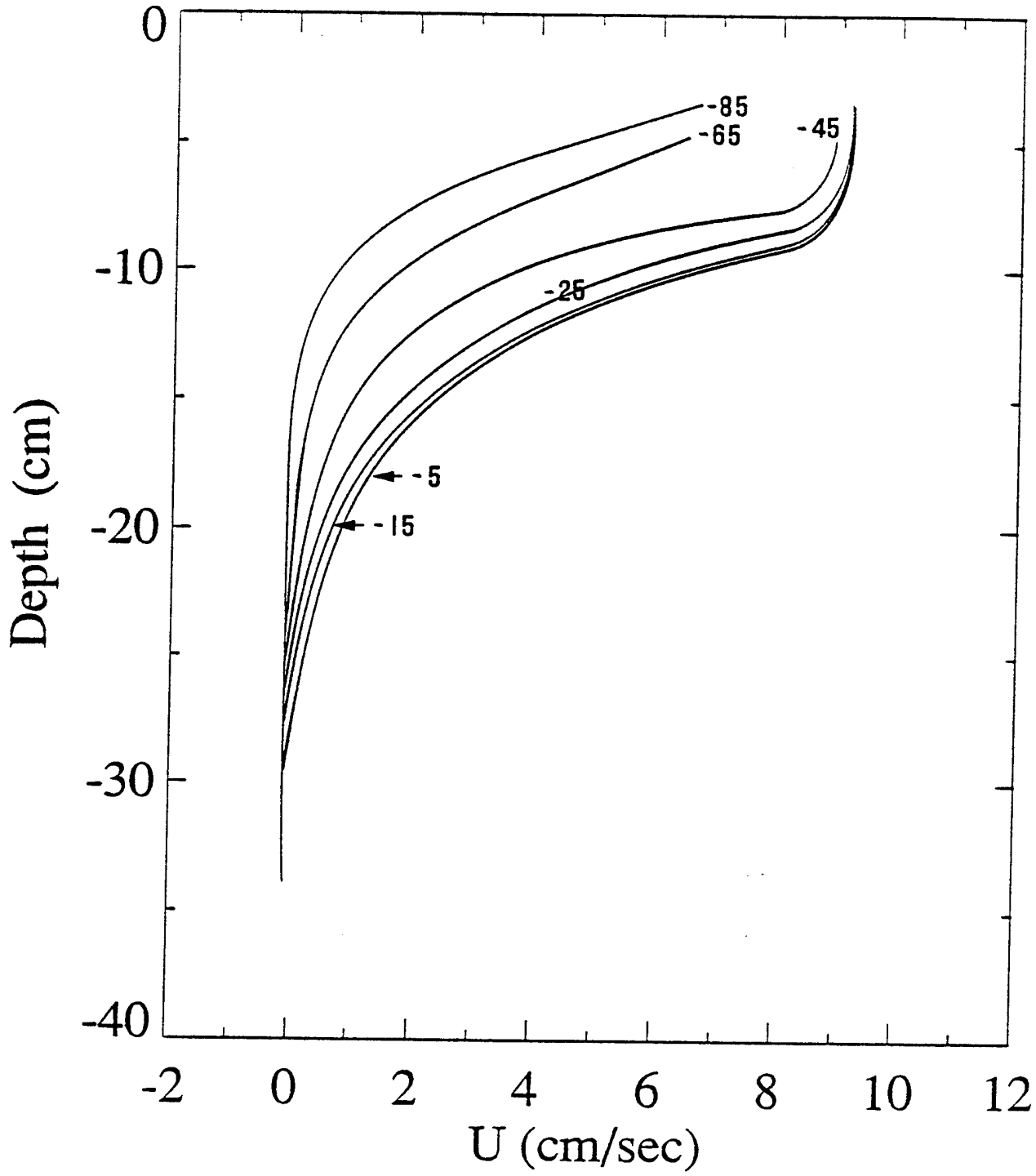

Figure 3. Evolution of the velocity profile in Run 151. Times shown are minutes before the start of the bottom floor. T = - 45 corresponds to the time the lid reached full speed.

(a)

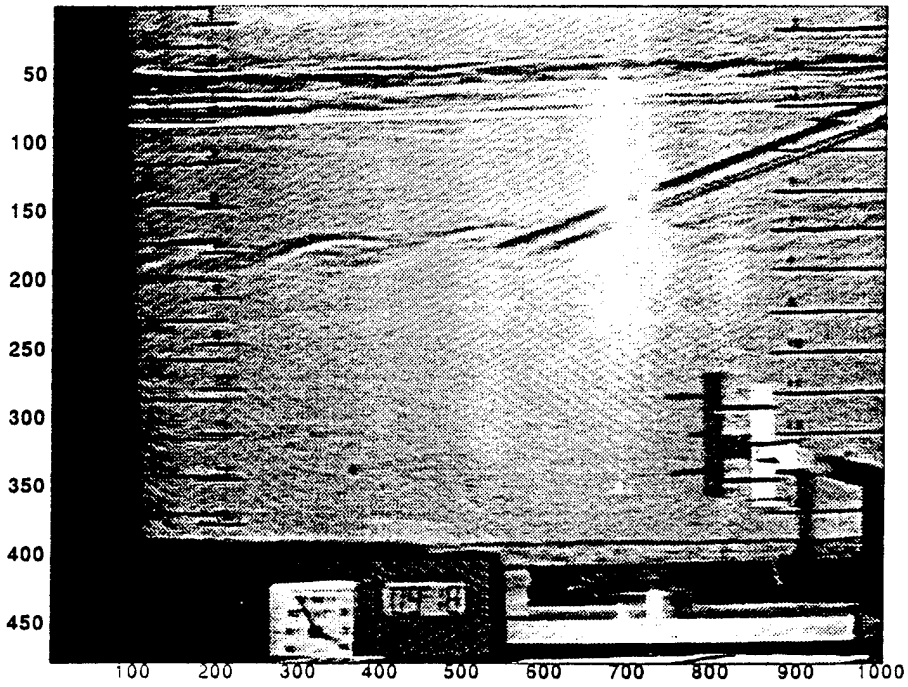

(b)

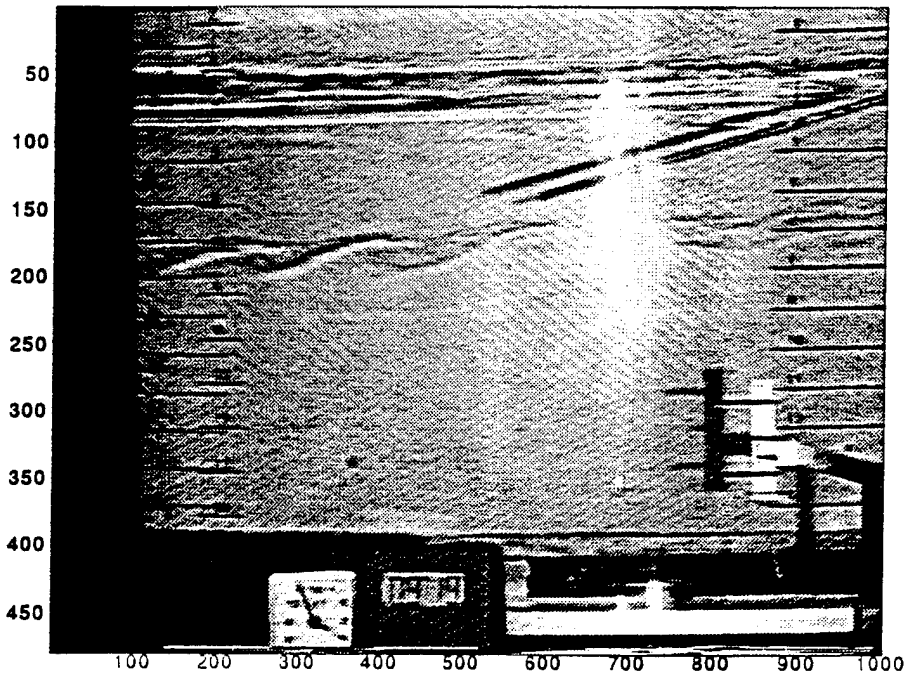

Figure 4. A series of enhanced video images from Run 171 showing the growth and decay of a series of Kelvin-Helmholtz billows. Times after the start of the experiment are (a) 9 minutes and 18 seconds (9:18), (b) 9:19, (c) 9:20, (d) 9:21, (e) 9:22, (f) 9:23, (g) 9:24, and (h) 9:25. In each image: a clock is shown at the bottom, scales (in inches) are shown on both the left and right hand edges, a bottom floor indicator is shown at the bottom right, the oscillating conductivity probe is shown extending into the image from the upper right corner, the bottom of the mixed region is shown at the top, and the reflection from the shadowgraph lamp is shown as the vertical spot to the right of the center of the image.

(c)

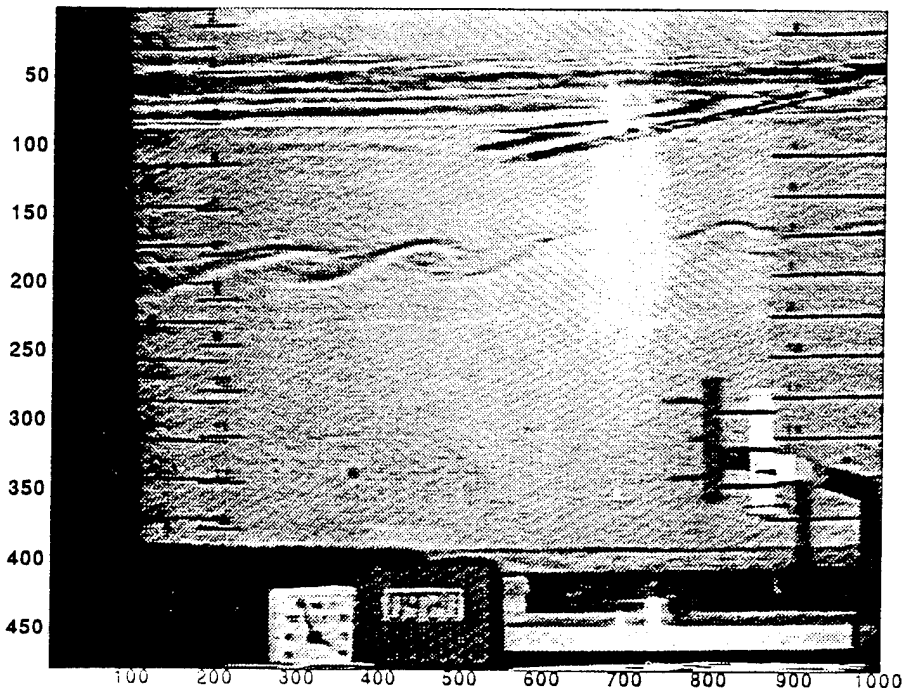
50
100
150
200
250
300
350
400
450
100
200
300
400
500
600
700
800
900
1000

(d)

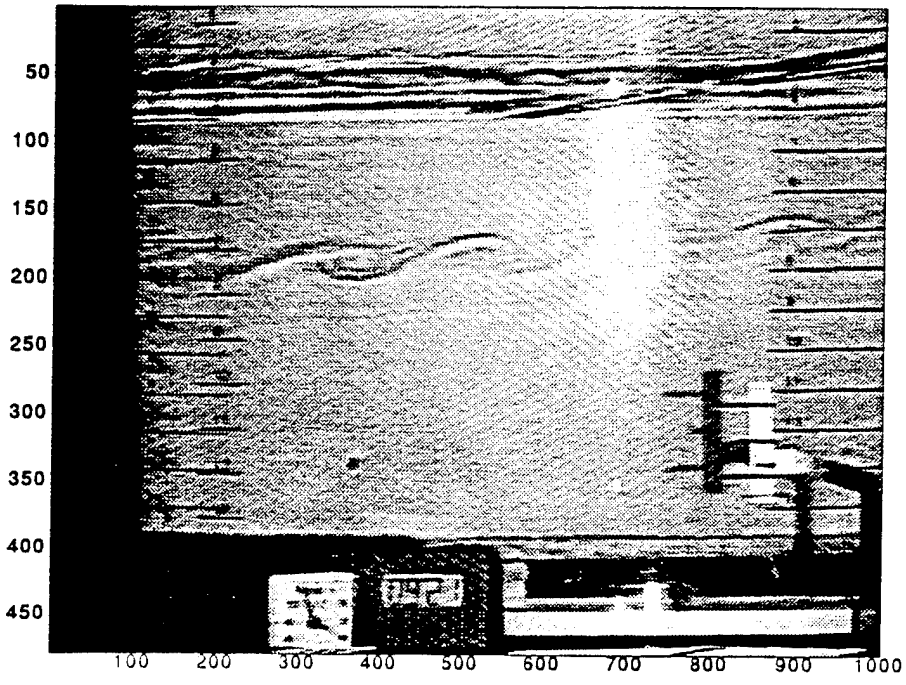
50
100
150
200
250
300
350
400
450
100
200
300
400
500
600
700
800
900
1000

(e)

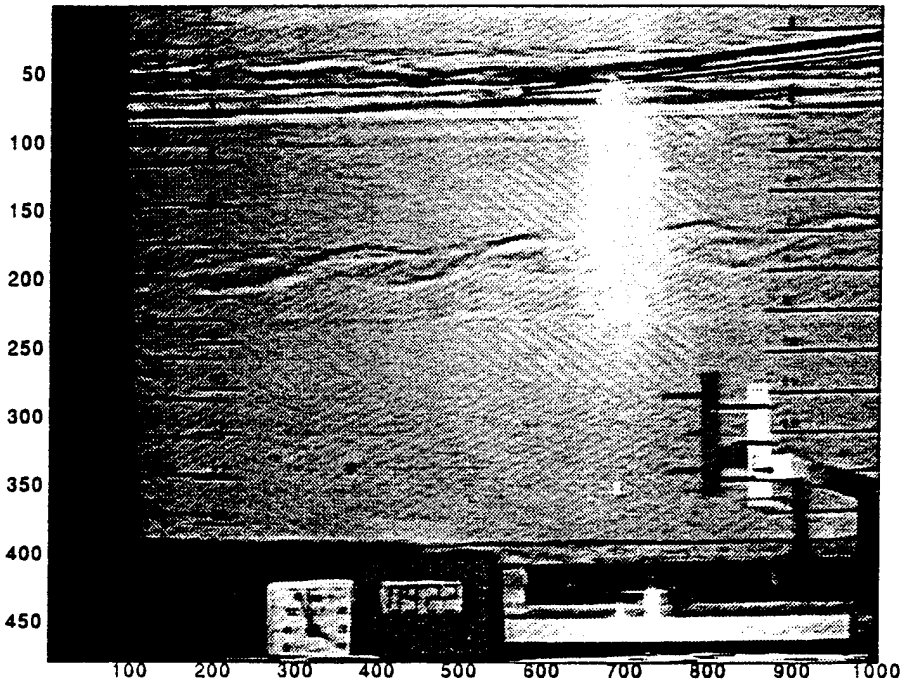
50
100
150
200
250
300
350
400
450
100
200
300
400
500
600
700
800
900
1000

(f)

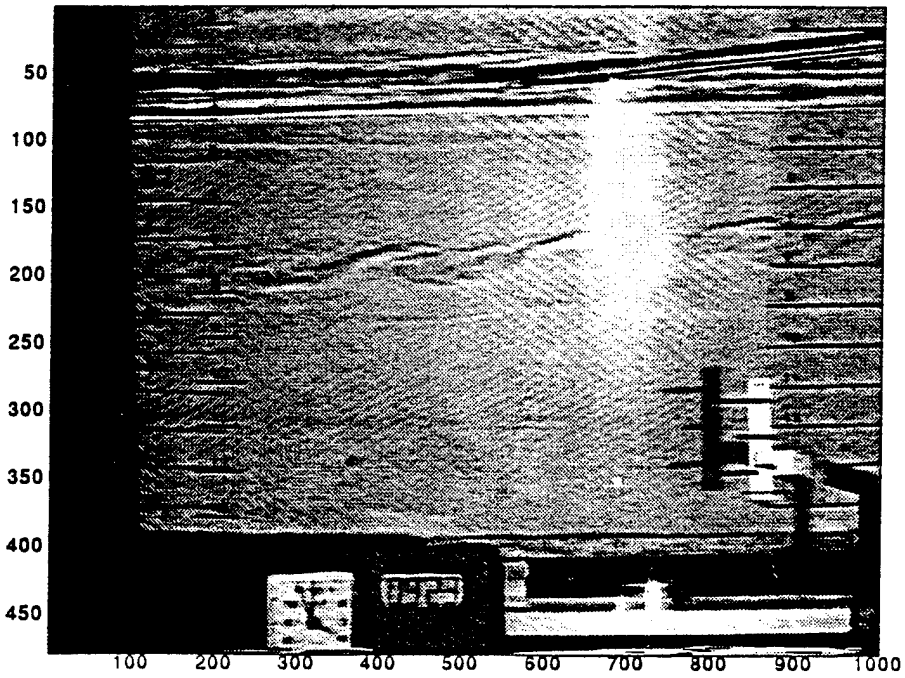
50
100
150
200
250
300
350
400
450
100
200
300
400
500
600
700
800
900
1000

(g)

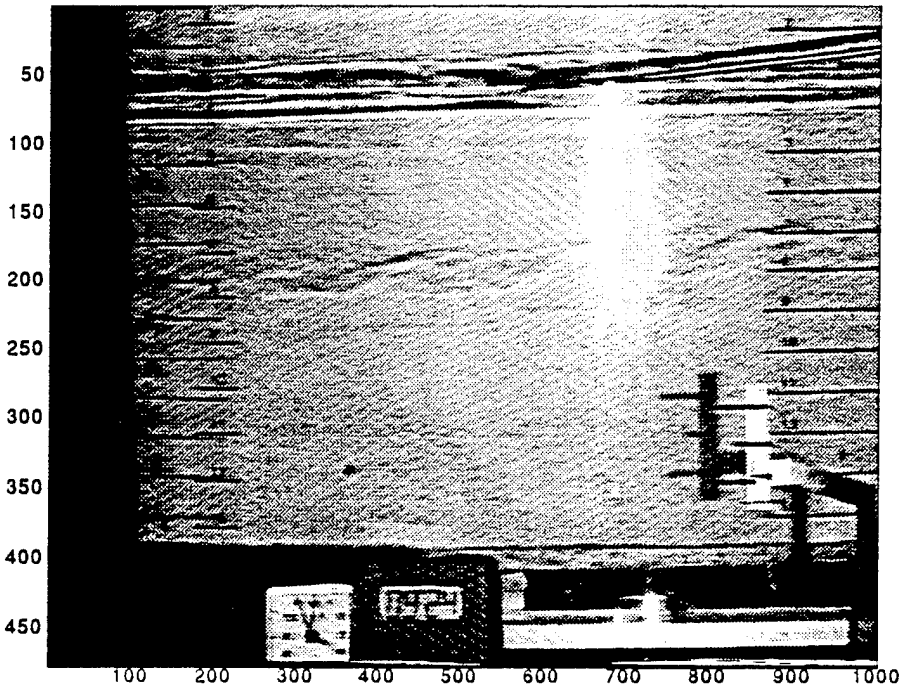
50
100
150
200
250
300
350
400
450
100
200
300
400
500
600
700
800
900
1000

(h)

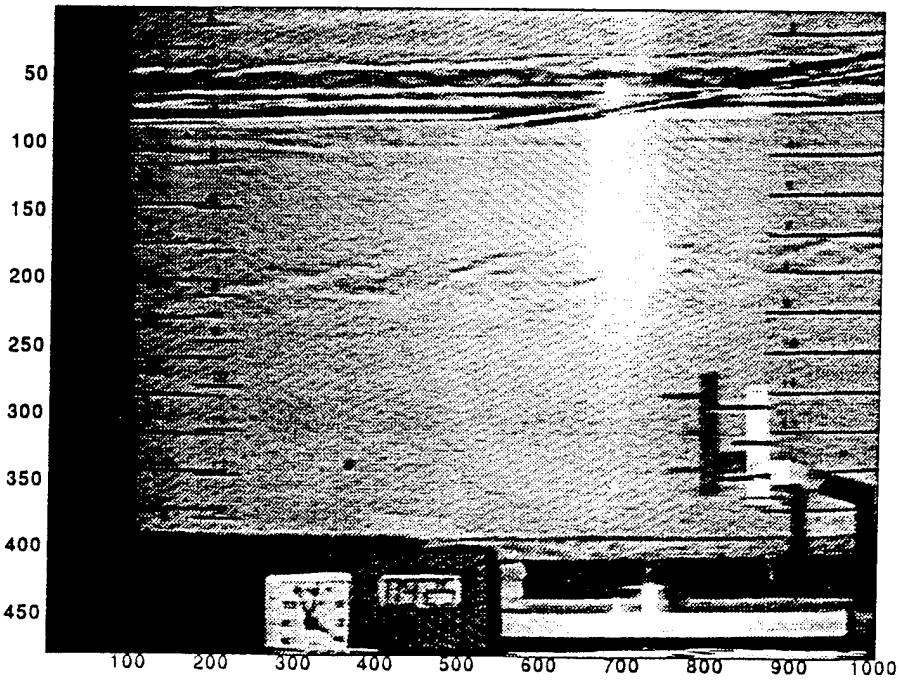
50
100
150
200
250
300
350
400
450
100
200
300
400
500
600
700
800
900
1000

vertically moving lever that is attached to the bottom floor in the center of the images. The white triangle just below the number "12" on the right-hand edge moves vertically with the floor. The white vertical strip on the tank wall shows the position of the floor. The horizontal, black lines on this strip mark the maximum (top) and minimum (bottom) positions of the floor. In Figure 4a, at 9:18, the floor is just below the non-deflected position. With each succeeding image, as time progresses, the indicator moves towards the trough of the wave. In the last image, at 9:25, the indicator is at the minimum position of the floor, i.e., at the trough of the wave. The oscillating conductivity probe is shown as the long, straight rod extending from the upper right corner of the image to near the center of the flow. The conductivity sensor is located at the end of this rod. The conductivity sensor moves vertically upwards with each succeeding photograph. The bottom of the mixed region is shown as the horizontal white and dark lines at a depth of around $3^1/_2$ inches below the surface. The shadowgraph lamp is reflected at the outer side wall of the tank and is the vertical white spot just to the right of the center in each image. Note that shadows from the bottom floor indicator and the conductivity probe are shown on the back wall of the tank.

In Figure 4, the region of interest is the flow at depths from 7 to 8 inches below the surface. In Figure 4a, this region shows a series of three waves at the depth of the conductivity sensor. As time progresses, these waves propagate to the right, and grow in amplitude into a series of overturning billows (Figures 4c and 4d at 9:20 and 9:21, respectively). The billows then collapse and finally decay (Figure 4h at 9:25). These waves look remarkably like Kelvin-Helmholtz billows which have been studied and documented in previous laboratory studies (Thorpe, 1968; Delisi and Corcos, 1973). We will show in the next section that quantitative measurements are consistent with this interpretation.

In some instances, we observed the K-H billows grow, then collapse and decay, and then grow again. An example of this is given in Figure 5 (from Run 141). This figure shows three enhanced video images similar to those in Figure 4. In Figure 5a, at a time of 5:43, the K-H billows have grown in amplitude and are starting to overturn. In Figure 5b, at 5:54, the waves have decayed, and the amplitudes are much smaller than in Figure 5a. In Figure 5c, at 6:04, the waves have grown again and are again overturning. This example is one in which waves grow, decay, and grow again. Although this phenomenon of growth, decay, and subsequent growth has been speculated on before, this is the first example in a laboratory experiment we have seen of its occurrence.

In Figure 6, we show more measurements of early K-H overturning. Figure 6a shows a shadowgraph image of overturning billows early in Run 151. Figure 6b shows the density profile at the same time from the oscillating conductivity probe. Also shown in Figure 6b, for comparison, is the initial density profile taken just before the start of the bottom floor. This figure shows that the overturning, at a depth of around 17 cm, occurs at the base of a region of weak density gradient. This result is consistent with our earlier findings and argues against convective overturning. We will return to this topic in Section 4.2 in our discussion of Figure 10.

At later times ($t > \sim 13$ - 16 minutes), the flow in the tank is characterized by one or more internal mixing regions (Delisi and Dunkerton, 1989 and 1994). These regions are characterized by lens-shaped masses of fluid which propagate around the tank at the speed of the bottom wave

(a)

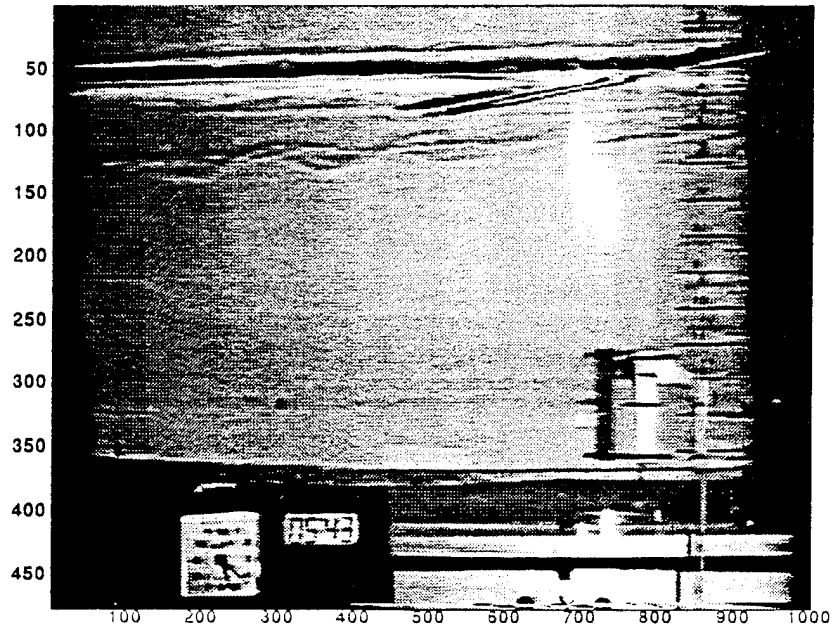

(b)

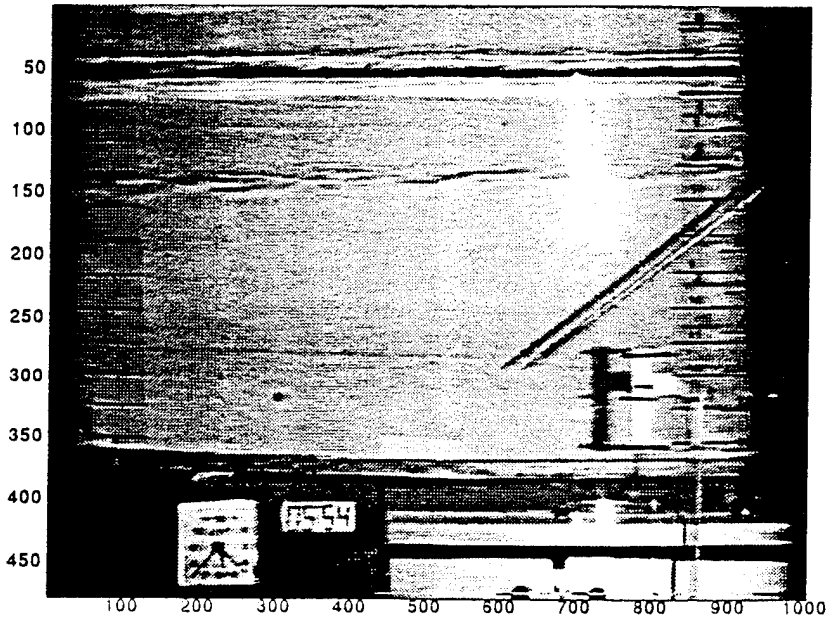

Figure 5. Three enhanced video images from Run 141 showing the growth (Figure a), collapse and decay (b), and re-growth (c) of K-H billows.

(c)

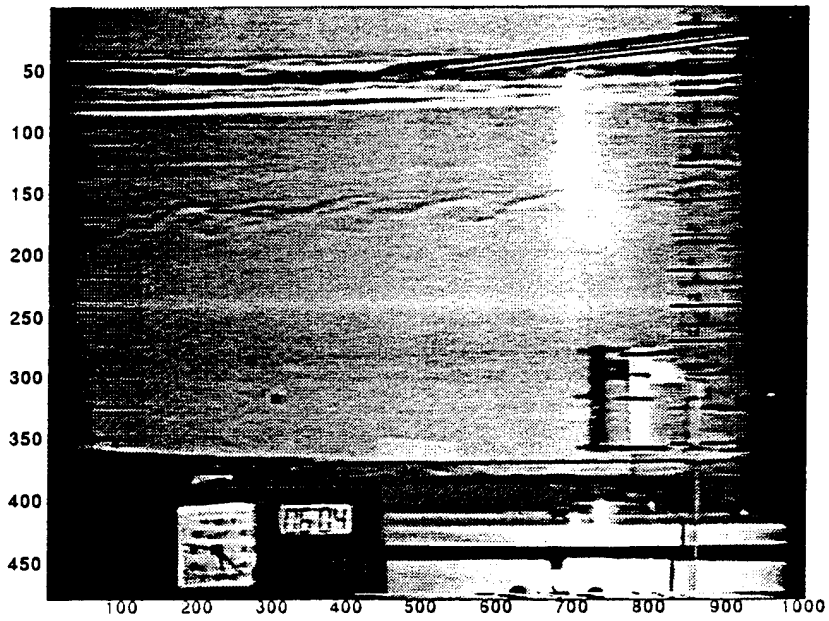
50
100
150
200
250
300
350
400
450
100
200
300
400
500
600
700
800
900
1000

(a)

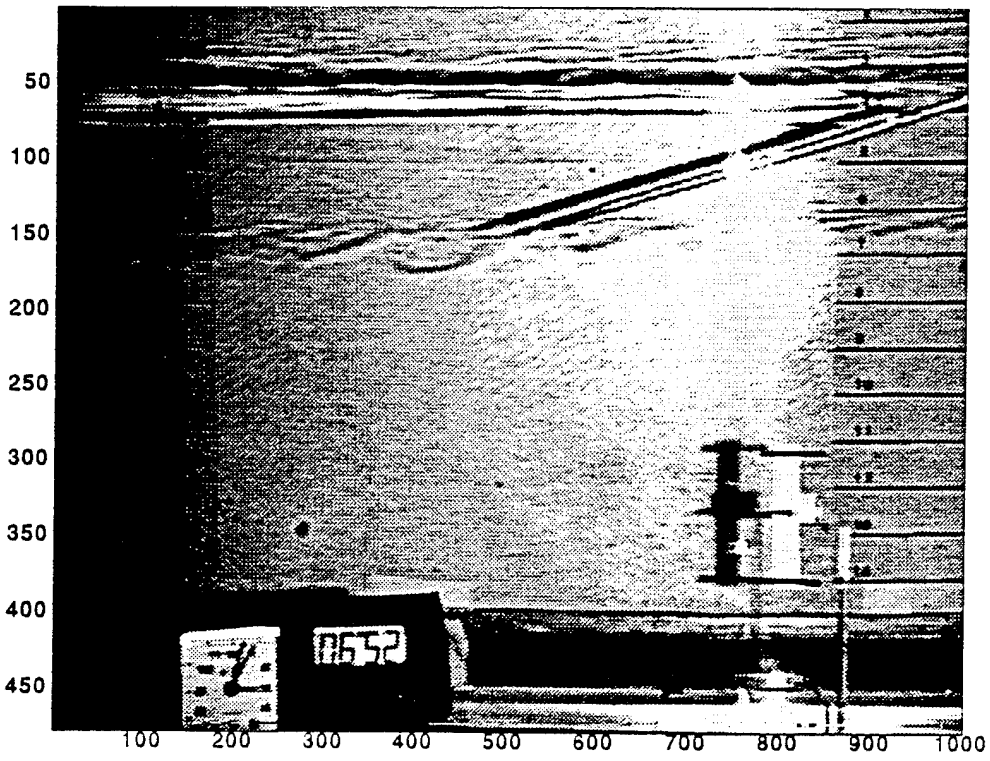

(b)

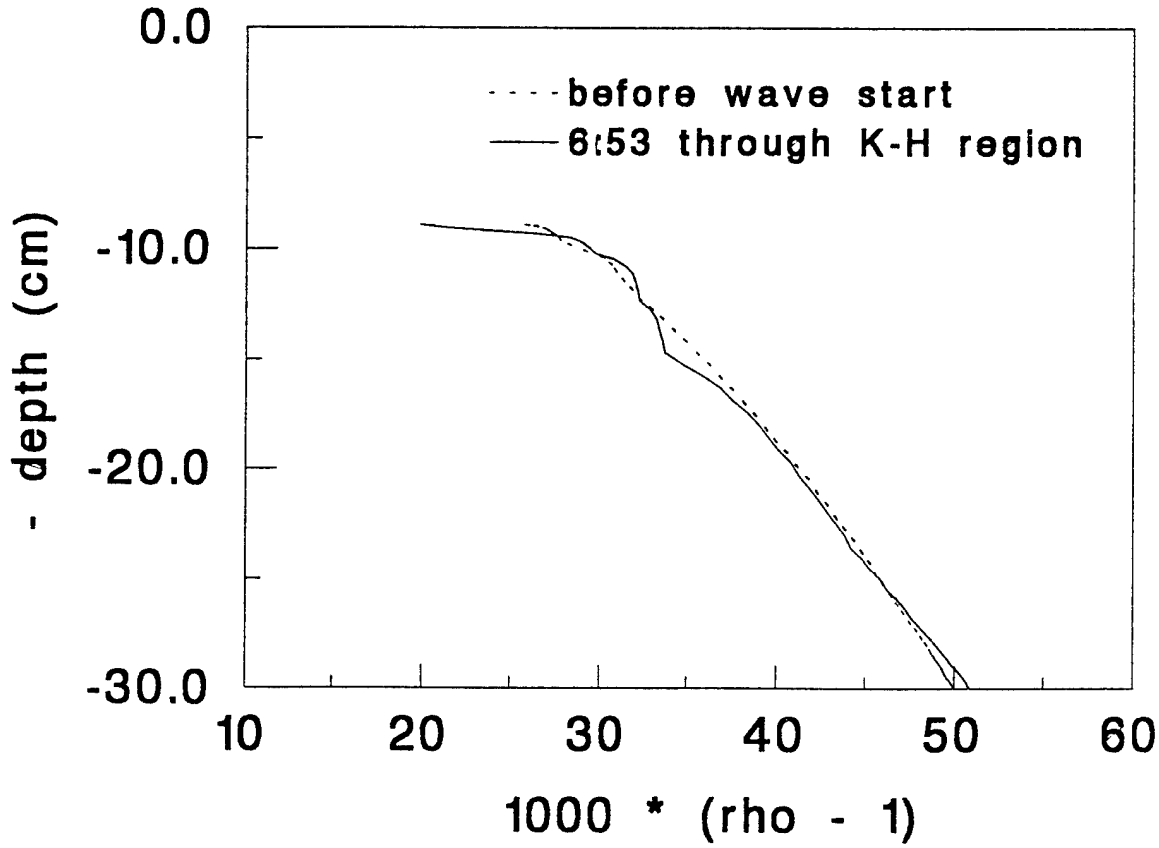

Figure 6. (a) An enhanced video image from Run 151 showing a series of K-H billows and (b) a simultaneous density profile from the oscillating conductivity probe through the same region.

in the single-wave case or at the speed of the composite wave in the two-wave case. More will be said about these regions in Section 4.3.

4.2 One-wave results

The results in this section will concentrate on those runs in which we used a single wave on the bottom floor.

Several runs were performed using a single, forcing wave on the bottom floor (see Table 1). Examples of the floor position for two of these runs are shown in Figure 7. In Figure 7a for Run 111, the floor was started at time = 0 with the full amplitude of 2 cm (4 cm peak-to-peak). This is termed a "hard start" of the floor. In Run 161, we performed a run identical to Run 111 only with a "soft start" of the bottom floor. In a soft start, the amplitude of the wave at the floor is initially zero and increases linearly with time until, at the end of 8 cycles, the amplitude of the bottom wave is 100 percent. The position of the bottom floor for Run 161 is shown in Figure 7b. We performed a "soft start" in this run because we believed there may be adverse side effects to starting the floor at the full amplitude. One such side effect was thought to be secondary harmonics. We will show in Figure 8 that these side effects appear to be negligible. Note that the final amplitude of the bottom floor in both Run 111 and 161 is 2 cm (4 cm peak-to-peak).

Videotapes of shadowgraph visualization clearly show the regions of overturning and turbulence as a function of time (cf., Figures 4, 5, and 6). We have analyzed these videotapes to determine the vertical extent of the breaking regions as a function of time for each run. Figure 8a shows the observed regions of turbulence vs. time after the start of the bottom floor for Run 111, and Figure 8b shows the same information for Run 161. Both of these figures show the following, similar features:

a. The initial regions of turbulence, from t = 0 to t ~ 13 – 16 minutes, first appear near the top of the tank and progress downwards, toward the bottom floor, as time increases.

b. For t > ~ 13 - 16 minutes, most of the observed turbulence occurs in mixing regions in the bottom third of the tank, with only sporadic, patchy turbulence being observed in the top half of the tank.

c. The major effect of the "soft start" in Run 161 is to delay the appearance of the first regions of turbulence. In Run 111, the first turbulence appears at t ~ 2 minutes. In Run 161, the first turbulence appears at t ~ 5 minutes. This delay was expected since the amplitude of the forcing wave, hence, the wave energy, takes longer to reach the steady-state value in Run 161. Note that the observed regions of turbulence for these two runs overlay each other nicely if one run is shifted 3 minutes relative to the other. This result implies that the "hard start" and "soft start" results are nearly identical except for a small shift in time.

(a)

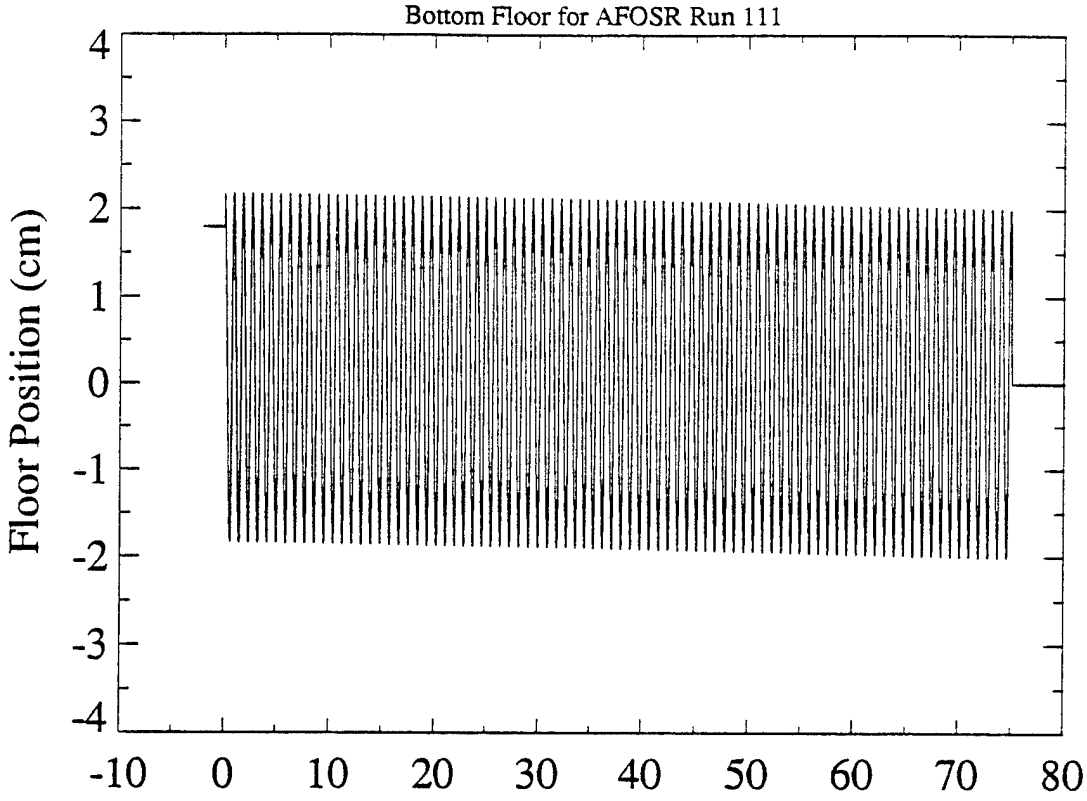

(b)

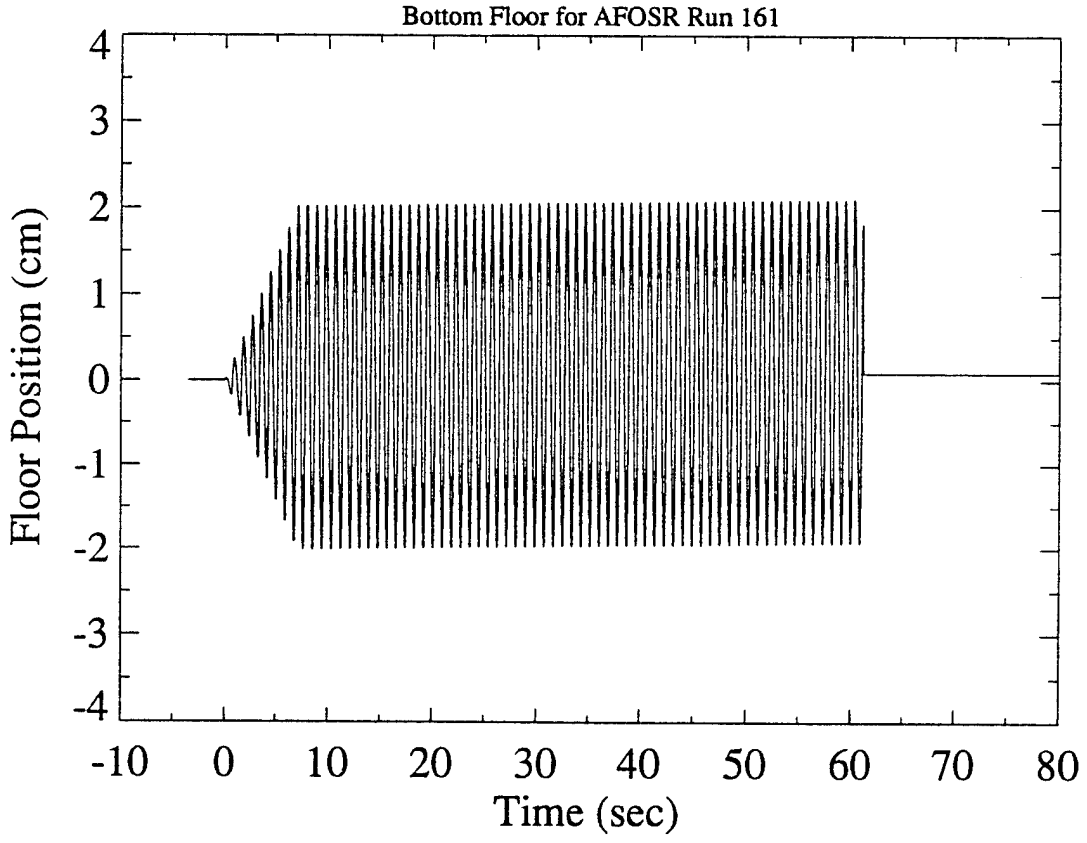

Figure 7. Floor position vs. time for two, one-wave runs: (a) Run 111 and (b) Run 161.

(a)

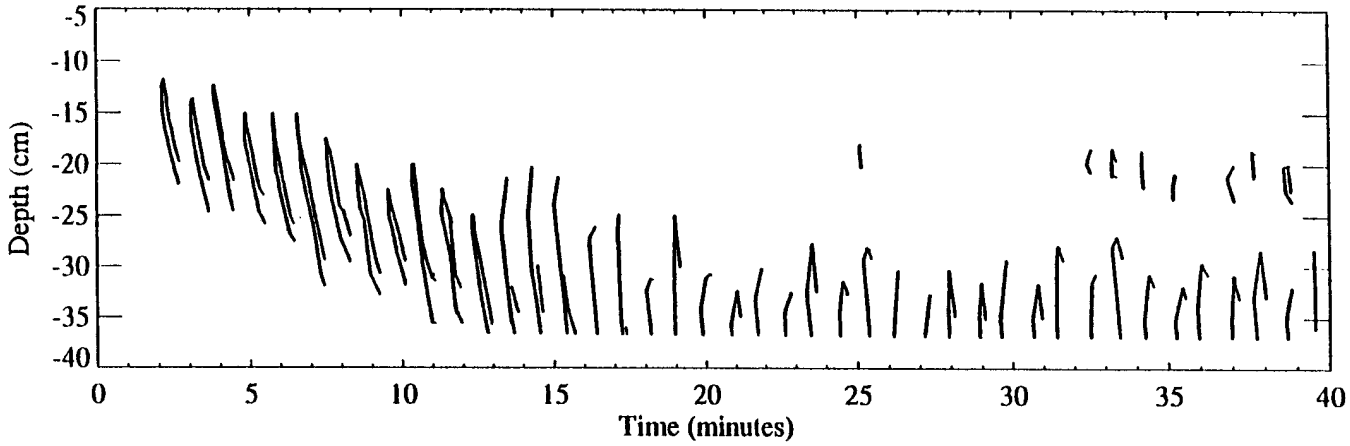

(a)

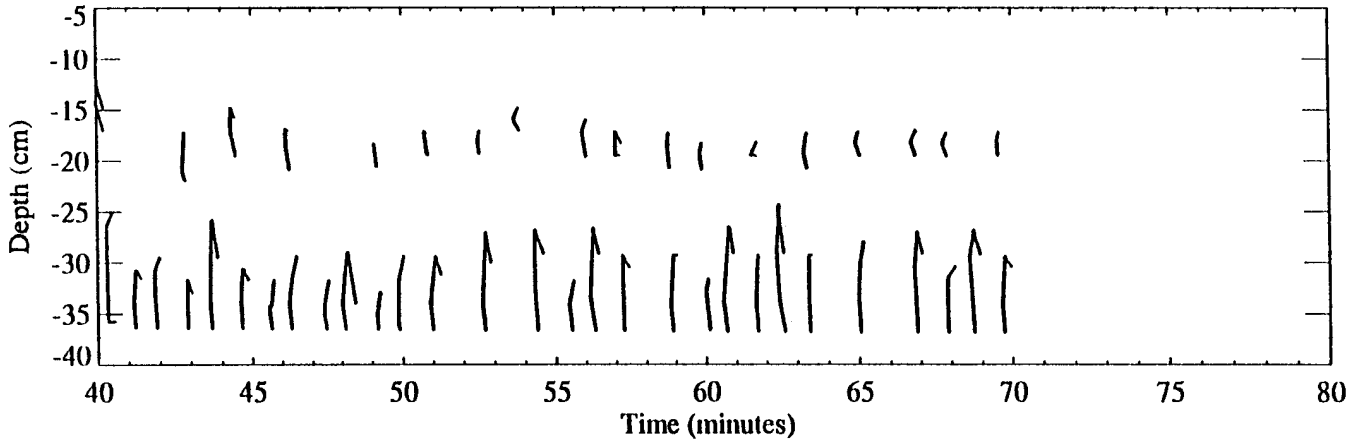

Figure 8. (a) Observed regions of turbulence in the one-wave experiment, Run 111. Time is minutes after the start of the experiment. (b) Similar to (a) except for Run 161.

(b)

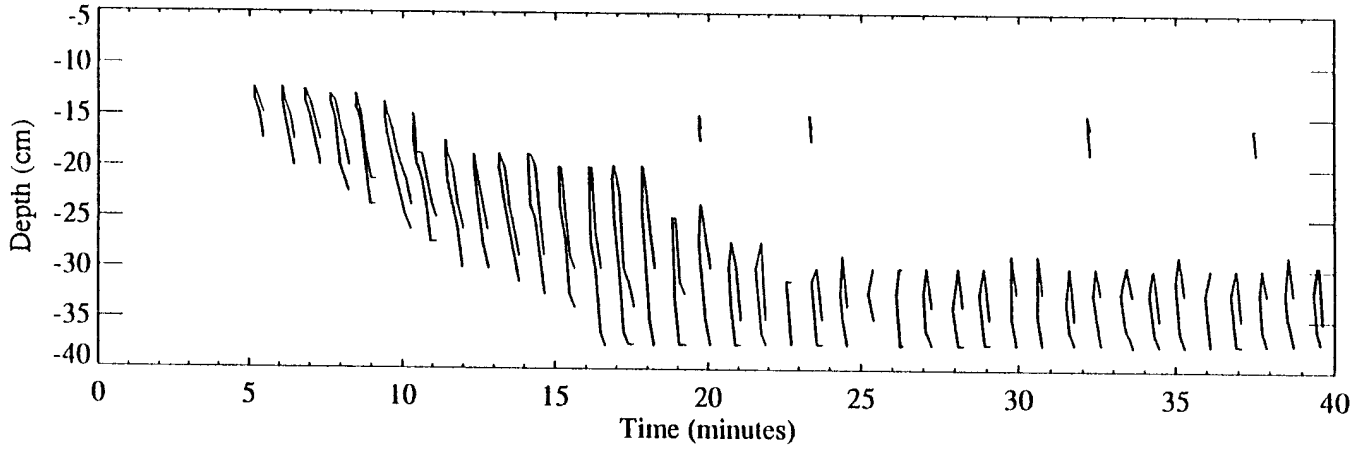
-5
-10
-15
-20
-25
-30
-35
-40
Depth (cm)
0
5
10
15
20
25
30
35
40
Time (minutes)

(b)

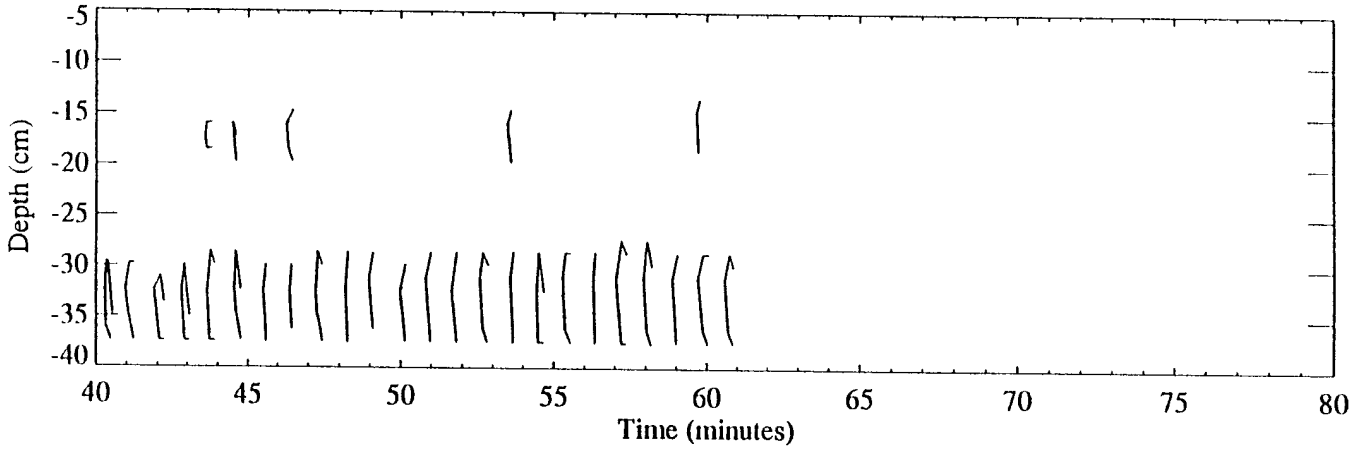
-5
-10
-15
-20
-25
-30
-35
-40
Depth (cm)
40
45
50
55
60
65
70
75
80
Time (minutes)

Instantaneous velocity profiles obtained from streak photographs were averaged over one wave cycle to estimate the mean velocity profile. Figure 9 shows the evolution of the mean velocity profile with time from Run 38, which is similar to Run 111 (figure from Delisi and Dunkerton, 1989). This figure shows that a ledge appears in the mean flow at t = 5 minutes, around the time of K-H overturning. By t = 10 minutes, this ledge has progressed downwards toward the floor of the tank, consistent with the activity plot in Figure 8a. At t = 20 and 75 minutes, the mean velocity profile is nearly constant with depth. During this time, the flow is dominated by the mixing regions in the lower part of the tank.

We have examined the instantaneous velocity and density profiles for Run 38 to estimate the Richardson number evolution in the early flow. The Richardson number is defined as

$$\mathrm{Ri} = \frac{N^2}{\left(\frac{\partial U}{\partial z}\right)^2} \qquad (3)$$

where N is the Brunt-Vaisala frequency (eqn. 1) and $\partial U/\partial z$ is the vertical shear. A region is linearly unstable if Ri < .25 (Miles, 1961; Delisi and Corcos, 1973).

Figure 10a (from Delisi, 1988) shows data from Run 38 from 4:25 to 7:55. The vertical lines in the figure are located at crests of the bottom wave. Constant density surfaces are shown from 10 to 25 cm depth, with the base of the mixed region at a depth of around 10 cm. Three regions of wavebreaking from the videos are shown as the shaded regions. In this figure, the breaking begins approximately 15 cm below the lid, near the trough of the bottom wave, and progresses lower in the tank during each wave cycle, similar to the data shown in Figure 8. The breaking occurs at the base of the weak gradient region in each cycle and just above regions of stronger density gradient. Several instantaneous velocity profiles, from streak photographs, are also shown in this figure. In each profile, the maximum instantaneous velocity shears are located vertically in the regions of wavebreaking. Below the critical level (which occurs at a depth of 11 - 12 cm), the maximum particle velocities are located above the regions of wavebreaking and are in the regions of weaker density gradient. Convective overturning will occur when the instantaneous particle speeds exceed the wave phase speed (Orlanski and Bryan, 1969). Hence, convective overturning will occur at vertical locations where the instantaneous particle speeds are a maximum, whereas here the overturning is observed below the locations where the particle speeds are a maximum. These results imply a K-H instability rather than a convective instability.

In Figure 10b, we plot the Richardson number for this data. To compute the Richardson number, we used the density contours in Figure 10a to compute a local N, and we used the streak photographs to compute $\partial U/\partial z$. Figure 10b shows that the Richardson number is low in the regions where we observe wavebreaking in Figure 10a. This wavebreaking occurs in regions of low N and high shear.

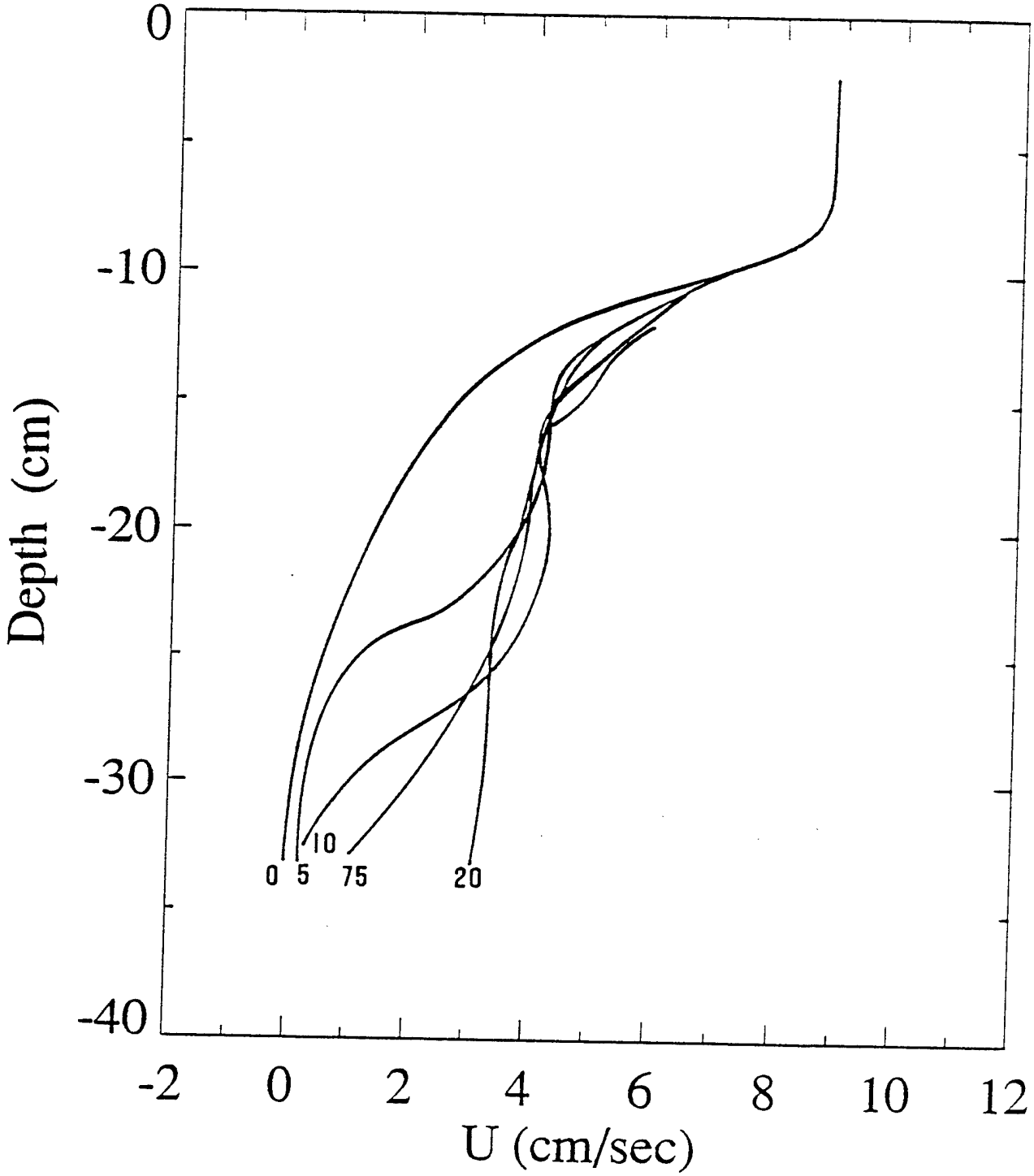

Figure 9. Evolution of the mean velocity profile with time in a one-wave experiment. Times are in minutes after the start of the bottom floor. (From Delisi and Dunkerton, 1989)

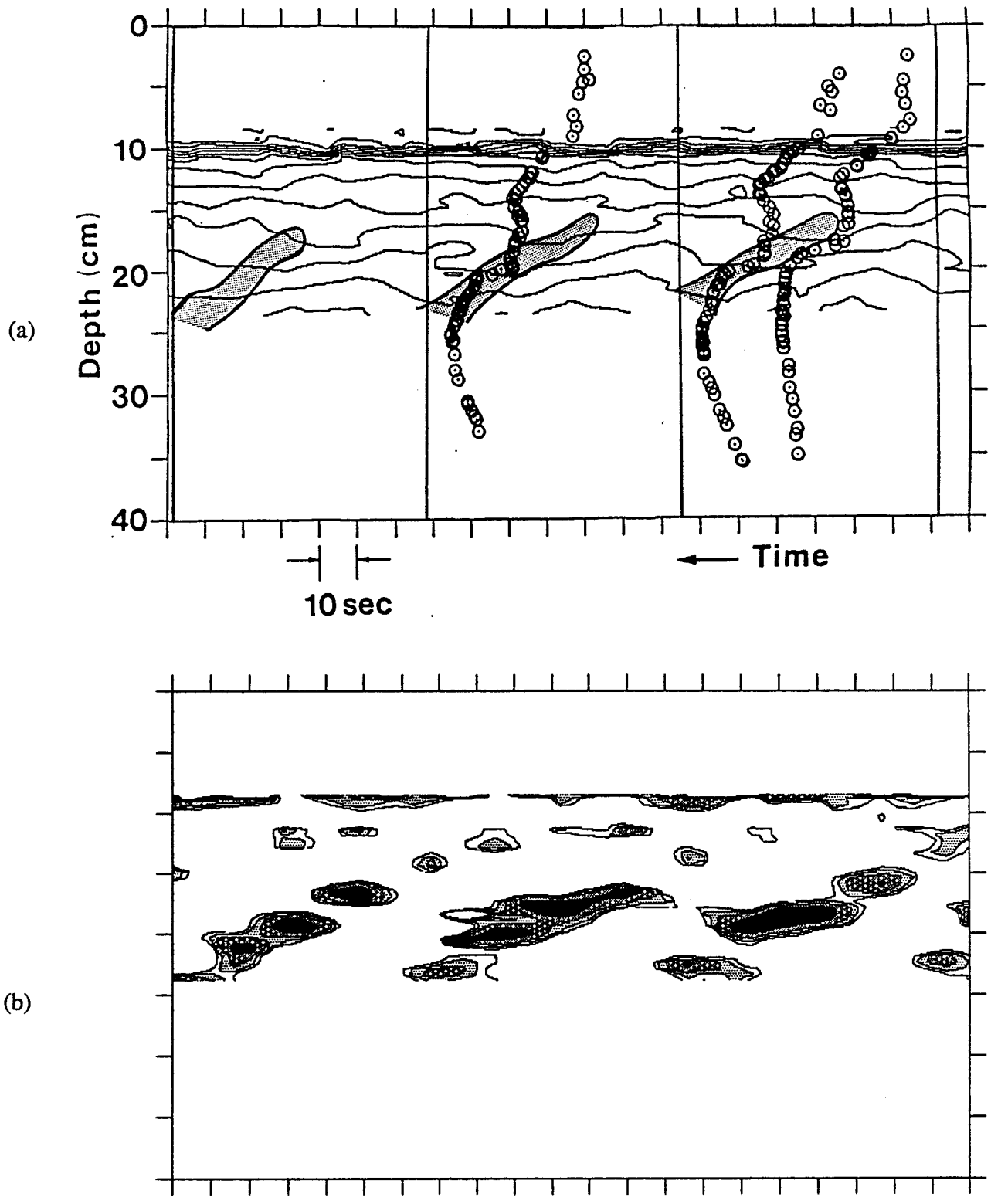

Figure 10. (a) Contours of constant density surfaces, regions of wavebreaking, and several instantaneous velocity profiles (Run 38 from 4:25 to 7:55). The vertical lines locate the crests of the bottom wave. (b) Richardson number estimates for the data in Figure 10a. The darkest area signifies Ri<1. Contour intervals are one unit apart.

Note that, from Fig. 3, at the depth of the critical level for the 4.5 cm/sec wave,

$$\frac{\partial U}{\partial z} \sim 0.93 \text{sec}^{-1} \qquad (4)$$

and the mean flow Richardson number is 1.2. This is the minimum Richardson number in the flow (at or below the critical layer), since the vertical shear gets weaker with increasing depth. At the depth of the observed overturning in Fig. 4, for example, ($z \sim 16.5$ cm) the mean flow Richardson number is over 8. Thus, the mean flow Richardson number is above one at the critical layer and increases rapidly with depth. The mean flow, then, is stable to Kelvin-Helmholtz instability. It is the wave shear, when added to the mean shear, which reduces the Richardson number below one-quarter, thereby generating overturning and turbulence. This is seen most clearly in Figure 10. Here, at a depth of 20 cm, the mean flow Richardson number is ~20. With the bottom wave forcing, however, the local Richardson number in the overturning region is ~ 0.05 (using the instantaneous velocity profiles shown in Figure 10). Thus the wave shear added to the mean shear reduced the local Richardson number below one-quarter.

To explore this phenomenon in more detail, we performed DPIV studies, as discussed in Section 3. Figure 11 shows a comparison of instantaneous velocity profiles from DPIV measurements and from tracking of individual particles taken before the start of Run 221. Two DPIV profiles are shown, made with different processing windows. The profile with the larger window shows a smoother profile and is more representative of how the particle tracking was performed. The profiles from both methods agree well to within a fraction of one cm/sec. This comparison shows that DPIV agrees well with individual particle tracking, which is similar to using particle streak photographs to determine instantaneous velocity profiles.

In Run 211, we co-located both the shadowgraph visualization system and the DPIV system. During selected times during this run, we turned off the shadowgraph and used DPIV to obtain data nearly simultaneously with the shadowgraph. Figure 12 shows a 35-mm photograph of early K-H overturning. Also shown is a vorticity plot using DPIV taken 1.8 seconds after the photograph. The DPIV imaging area matches the box outlined in black in the photograph. Because of difficulties obtaining a uniform particle distribution with depth, particle images could only be processed in a region $10.0 < z < 16.0$ cm, where $z = 0$ corresponds to the bottom edge of the box, which is a depth of 30.5 cm below the surface.

The K-H billows in the photograph are moving to the right at a speed of around 4 cm/sec. Because of the 1.8-second gap between the photograph and the vorticity plot, the rolling billow to the right of center in the viewing window in the photograph has moved to the far right in the vorticity plot. The billow just to the left of the center in the viewing window in the photograph has moved just to the right of center in the vorticity plot, and the vorticity concentration to the left of center in the vorticity plot is associated with a new billow, which is seen just to the left of the window in the photograph.

A shadowgraph visualization is an integration through the entire tank, from the outer side wall of the tank, where the light enters, to the inner side wall of the tank, where we observe the visualization. DPIV, on the other hand, measured the velocities on the centerline of the tank. The purpose of taking near-simultaneous shadowgraph and DPIV measurements, as in Figure 12,

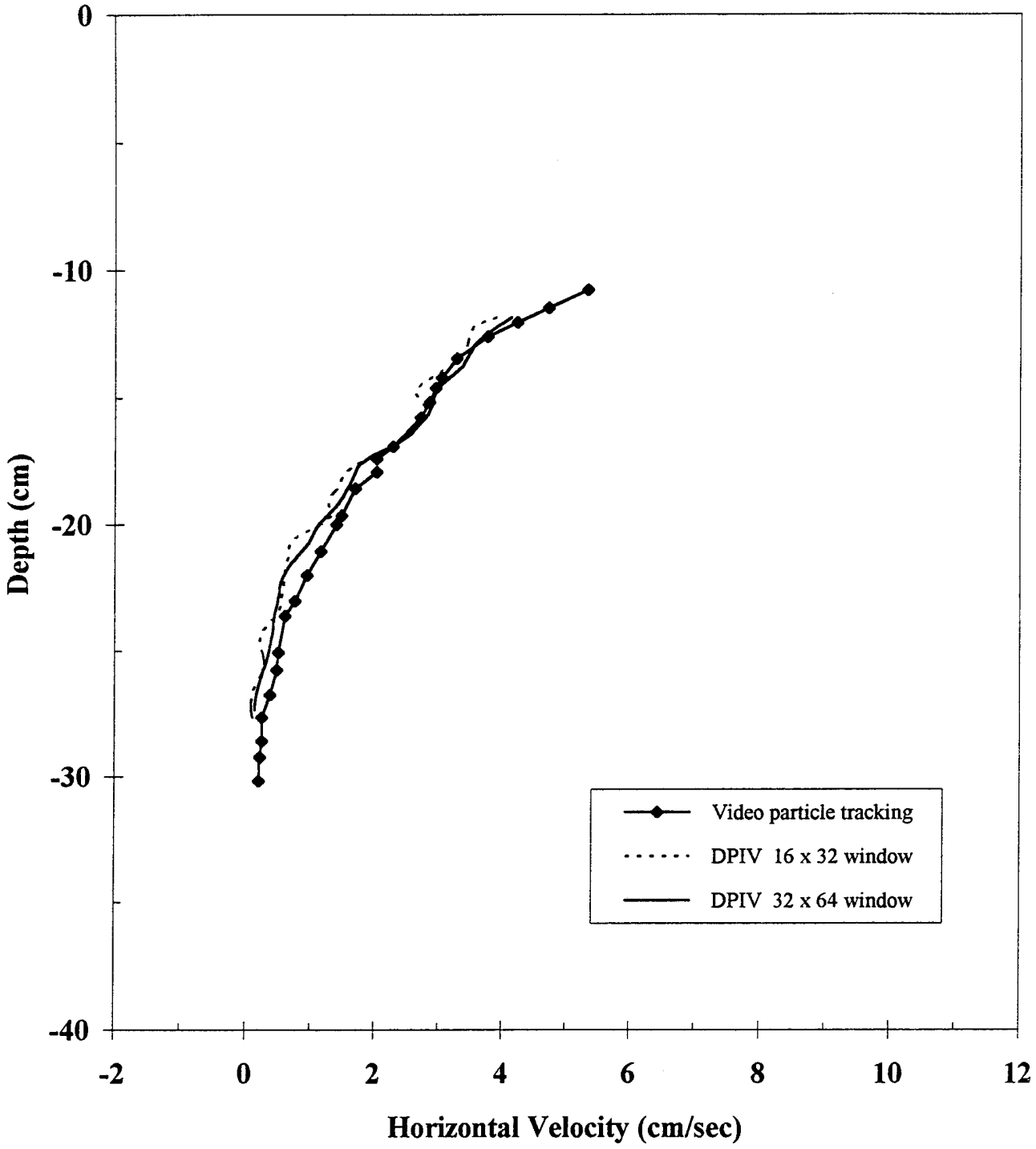

Figure 11. Comparison of instantaneous velocity profiles from DPIV measurements and from tracking of individual particles taken before the start of Run 221.

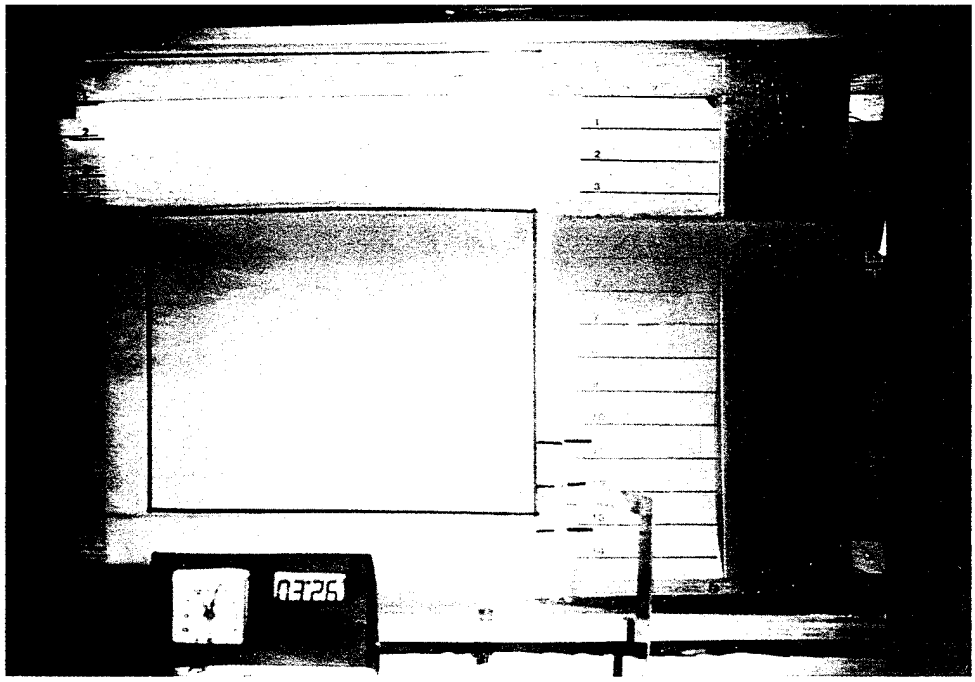

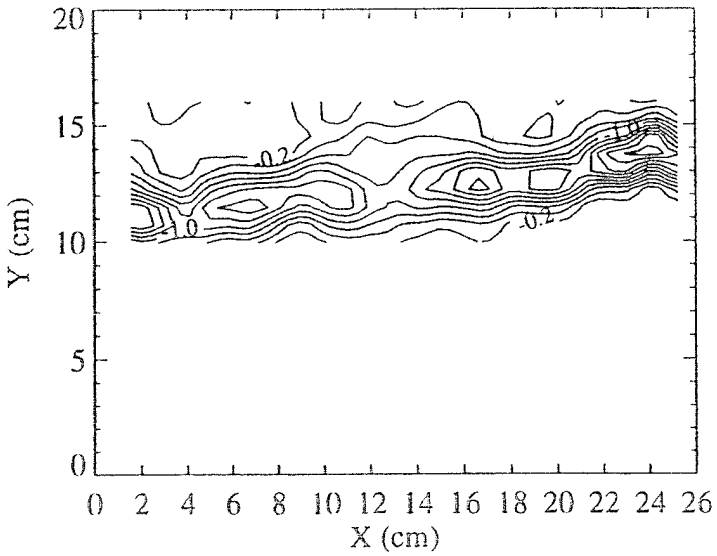

Figure 12. Photograph of shadowgraph visualization of K-H billows in Run 211 and a vorticity plot of the windowed area in the photograph using DPIV measurements taken 1.8 seconds after the photograph.

was to convince ourselves that the DPIV measurements were observing similar phenomena as we observed with the shadowgraph. This appears to be the case, since, from the DPIV measurements, we observed concentrations of vorticity in appropriate places, as visualized with the shadowgraph. This implies that the K-H billows were located in the center of the tank and were not simply a tank-wall phenomenon.

In Run 221, we obtained DPIV measurements at 4-second intervals over several cycles of the bottom wave. By linking together data from these consecutive images, we can study the gravity wave, critical layer interactions over a complete wave cycle. Figure 13a shows a composite view of vorticity over 1.5 wave cycles using 22 such images at an early time in the K-H overturning (8:05 - 9:29). Again, z = 0 corresponds to a depth of 30.5 cm below the surface. This composite was obtained by joining individual images edge to edge so that the central 18 cm were used from each image (corresponding to the distance the 4.5 cm/sec bottom wave travels in 4 seconds). This composite of images taken at a fixed location at many times may be thought of as an instantaneous image in the tank at one instant in time. A wave crest passed by the measurement station in the tank at times corresponding to x = 15 and x = 255 cm in the figure.

Figure 13b shows the evolution of the instantaneous horizontal velocity profiles measured in the center of each DPIV image used to compose Figure 13a. In this figure, z represents vertical position, as in Figure 13a, and the x-coordinate is a velocity scale representing 2 cm/sec between tick marks.

During Run 221, we also videotaped the particle field illuminated by the DPIV laser sheet. As in Figure 8, we observed this video and measured the depths and times of wavebreaking and rolling motions. These depths and times for Run 221 are shown in Figure 13c.

Figure 13 shows that the region containing vorticity descends with time at an angle of $\sim 2.9°$. The area containing the significant vorticity corresponds to the ledge of maximum velocity shear (Figure 13b) which also descends with time. As the velocity ledge descends, the maximum shear increases, until it is a maximum near 155 cm. Shortly after this, wavebreaking is observed (Figure 13c). The ledge in the velocity profile then relaxes, and the profile becomes nearly constant. At the start of the next cycle, a new velocity ledge forms, and the process repeats itself.

Figure 14 shows similar data to Figure 13 for motions 35 minutes after the start of the bottom wave. The data shown here are for one cycle from 35:09 to 36:05. During this time, a wave crest is at x = 133 cm. Here, the region containing negative vorticity descends at a slightly steeper angle of $\sim 3.5°$. A velocity ledge begins to form around x = 80 cm, but it is weaker and more vertically diffuse than in Figure 13. The most notable feature in the flow is the appearance of a jet of fluid moving at the phase speed of the bottom wave. The jet appears at $x \sim 131$ cm, and is nearly coincident with the crest of the bottom wave. This feature is most visible at z = 7.5 cm in the ninth (from the left) velocity profile in Figure 14b and as the left-most tip of the observed wavebreaking region in Figure 14c. Strong negative vorticity is observed along the lower edge of this jet, and wavebreaking continues along this lower edge well after the jet has passed.

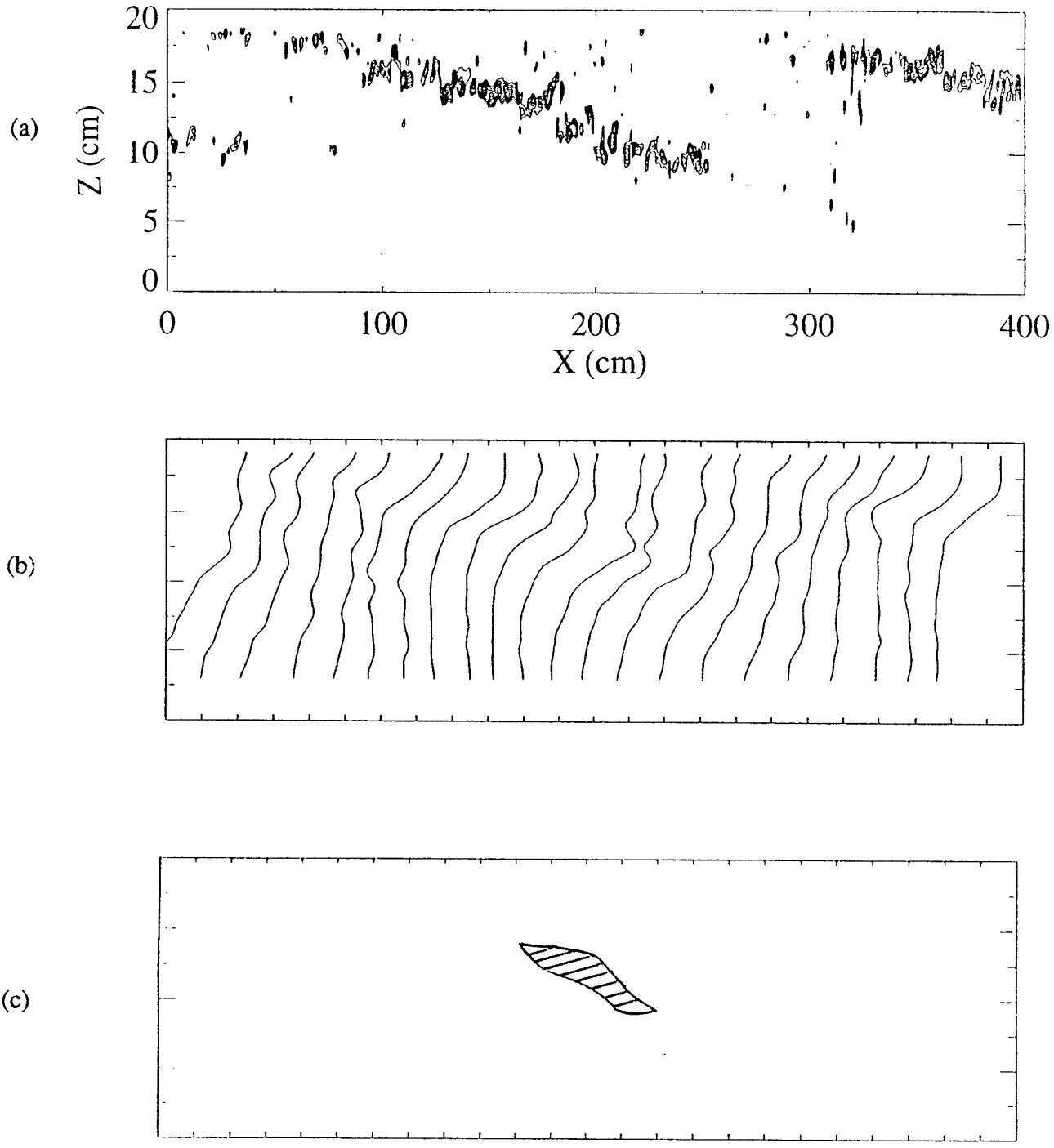

Figure 13. (a) Composite view of vorticity from DPIV images over 1.5 wave cycles at an early time in the K-H overturning (8:05 to 9:29) in Run 221. (b) Evolution of the instantaneous horizontal velocity profiles measured in the center of each DPIV image used in (a). (c) Observed regions of turbulence in Run 221 at the times shown in Figures 13a and 13b.

(a)

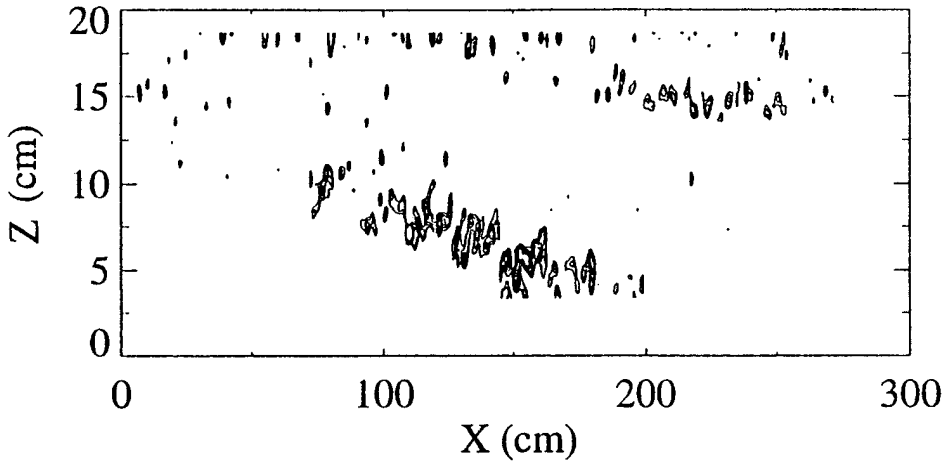

(b)

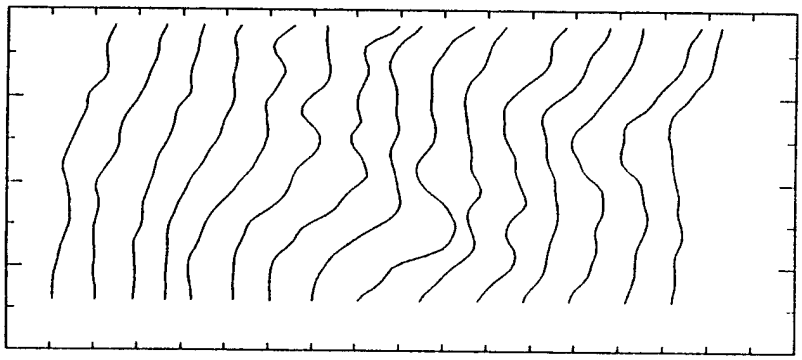

(c)

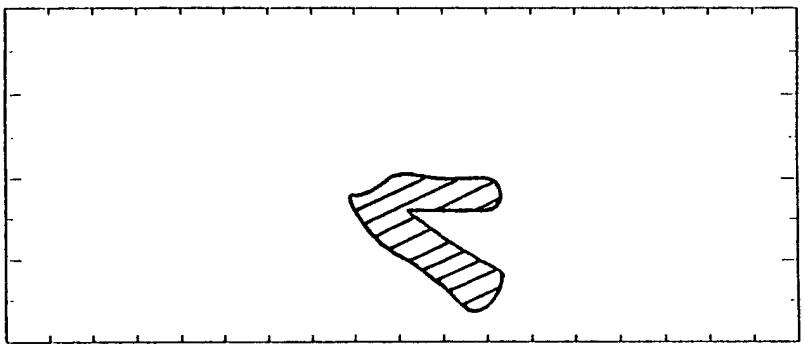

Figure 14. Similar to Figure 13 except only one wave cycle is shown at a later time in Run 221 (35:09 to 36:05).

Figure 15 shows the individual velocity profiles in Figures 13b (one cycle only) and 14b overplotted with a dark line representing the average velocity profile over the wave cycle. In both cases, the deviations from the mean during one wave period are significant, indicating that the gravity wave has significantly perturbed the mean flow. Also, note that in each wave cycle, the maximum velocity is nearly equal to the phase velocity of the bottom wave (4.5 cm/sec).

4.3 Two-wave results

Several two-wave experiments were performed in addition to the one-wave experiments described above (cf., Table 1). Because the waves had different phase speeds, the waves had different critical levels. Both waves always propagated in the same direction on the bottom floor.

In the first case to be discussed, Run 171, we used one wave with a phase speed of 4.5 cm/sec and a peak-to-peak amplitude of 4.0 cm and a second wave with a phase speed of 3.5 cm/sec and a peak-to-peak amplitude of 1.0 cm. (With these two waves, the bottom forcing has a beat period of 4 minutes.) Thus, this case is identical to the one-wave case (Runs 111 and 161) except for the addition of the small-amplitude second wave.

The floor position vs. time and the observed regions of turbulence for Run 171 are shown in Figures 16 and 17, respectively. (This run was terminated prematurely at 38:40 due to mechanical problems with the bottom-wave generators.) Figure 16 shows that the addition of the second wave causes a significant perturbation on the motion of the bottom floor relative to the one-wave case (Figure 7b). In both the one-wave case and this two-wave case, the initial K-H overturning is similar.

At $t > \sim 16$ min, the shadowgraph visualization for this run (Figure 17) shows a significant difference from the one-wave case (Figure 8b). In the one-wave case, the internal mixing regions which occur near the bottom of the tank appear once every wave cycle. Only small, sporadic regions of turbulence appear above these regions, at depths around 15 cm. In the two-wave case, around $t \sim 16$ min, the turbulent regions appear to bifurcate, with K-H overturning appearing at a depth around 17 cm and mixing regions, similar to those in the one-wave case, appearing at lower depths.

Although the time-averaged amplitude over one beat period is slightly higher in this two-wave run (1.30 cm peak-to-peak) vs. the one-wave run (1.28 cm/sec for Run 161), the observed regions of turbulence in the later flow are slightly more irregular in the two-wave case (cf., Figure 8b vs. Figure 17). This irregularity can be traced to the smaller floor motion at these times. Note, for example, the weaker flow signal in the bottom of the tank in Figure 17 at times 22:30, 26:30, 30:00, and 35:00. Referring to Figure 16, these are all times at which the bottom floor had a minimum excursion from the neutral floor position. Thus, the occurrence of the bottom mixing region appears to be connected to the local amplitude of the bottom wave forcing.

Run 191 is identical to Run 171 except we increased the amplitude of the second wave (again with a phase speed of 3.5 cm/sec) to a peak-to-peak amplitude of 2.0 cm. The floor position vs. time and the observed regions of turbulence for this run are shown in Figures 18 and 19, respectively.

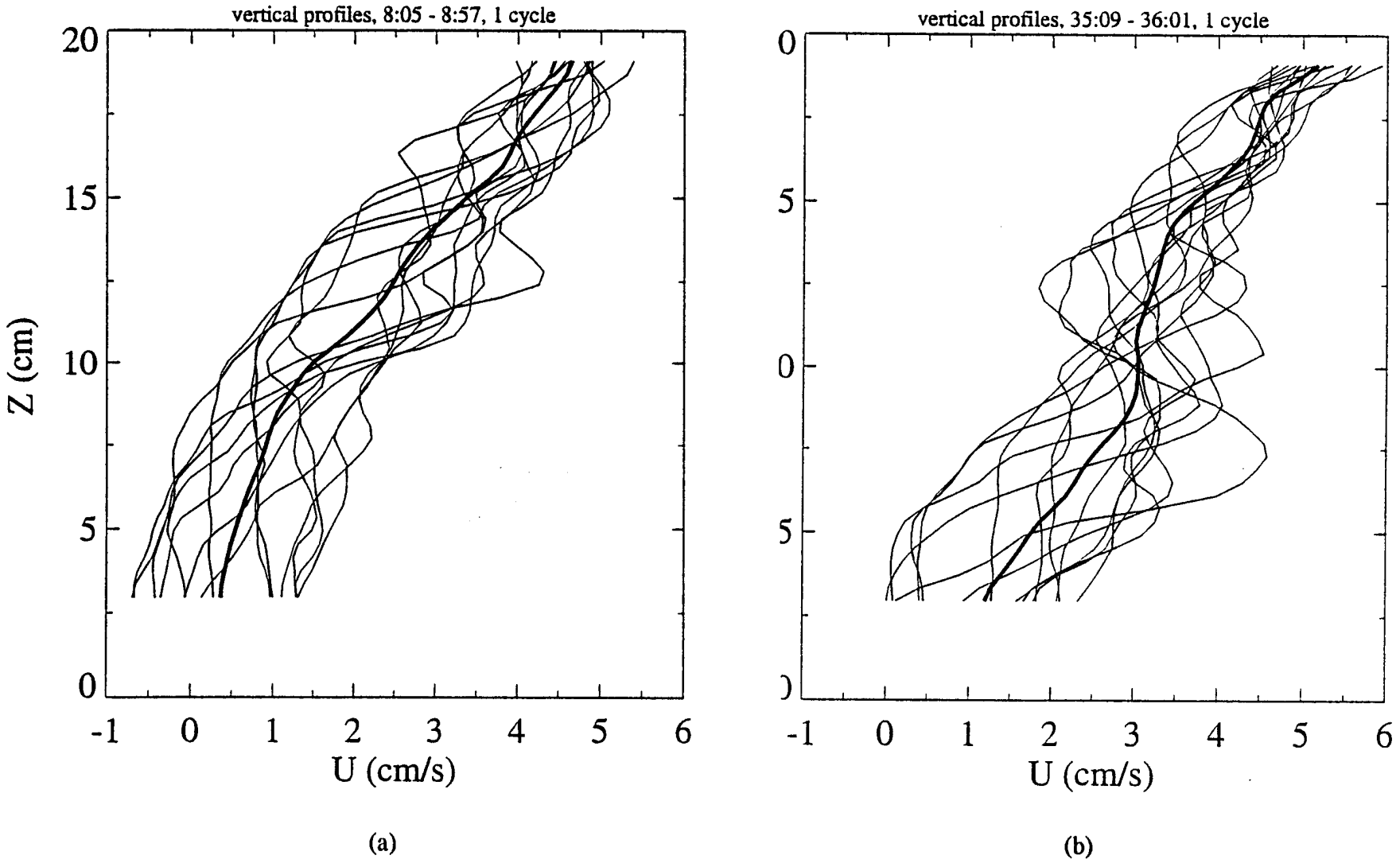

Figure 15. Instantaneous DPIV velocity profiles and the average (dark line) for (a) early wavebreaking from 8:05 to 8:57 and (b) late mixing region formation from 35:09 to 36:01 in Run 221.

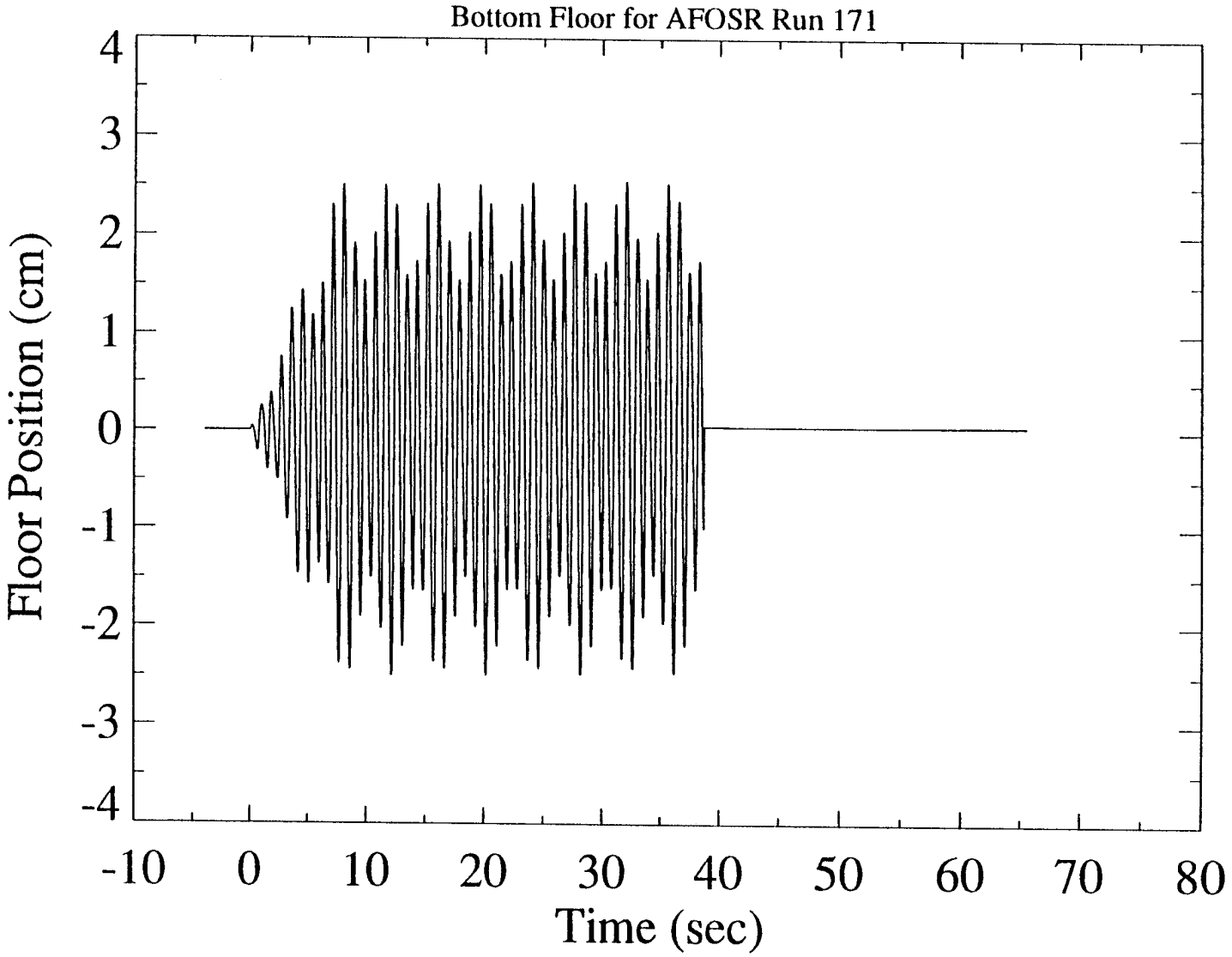

Figure 16. Floor position vs. time for Run 171 (a two-wave run with Wave 1 having a phase speed of 4.5 cm/sec and a peak-to-peak amplitude of 4.0 cm and Wave 2 having a phase speed of 3.5 cm/sec and a peak-to-peak amplitude of 1.0 cm).

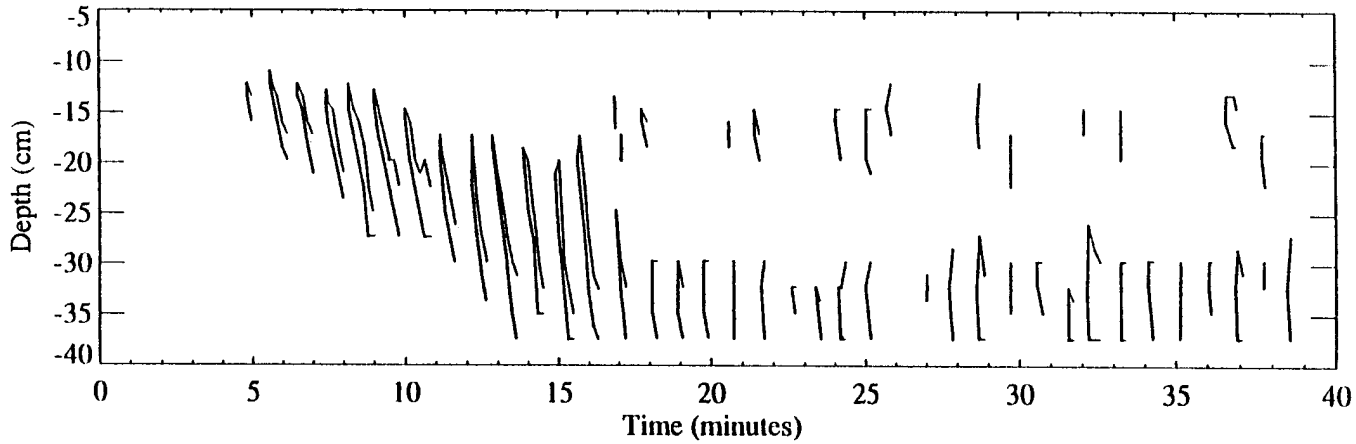

Figure 17. Observed regions of turbulence for Run 171 (a two-wave run with Wave 1 having a phase speed of 4.5 cm/sec and a peak-to-peak amplitude of 4.0 cm and Wave 2 having a phase speed of 3.5 cm/sec and a peak-to-peak amplitude of 1.0 cm).

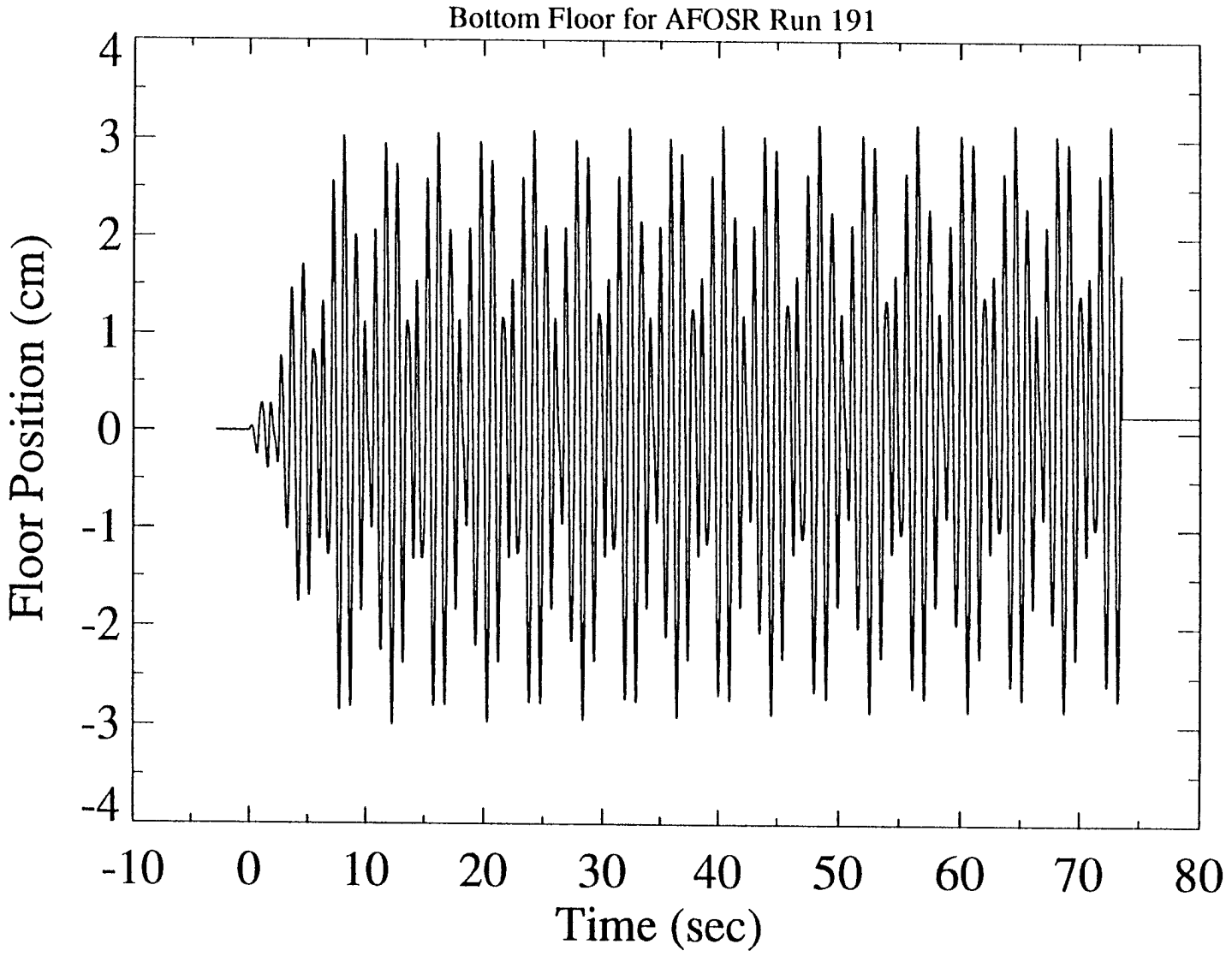

Figure 18. Floor position vs. time for Run 191 (a two-wave run with Wave 1 having a phase speed of 4.5 cm/sec and a peak-to-peak amplitude of 4.0 cm and Wave 2 having a phase speed of 3.5 cm/sec and a peak-to-peak amplitude of 2.0 cm).

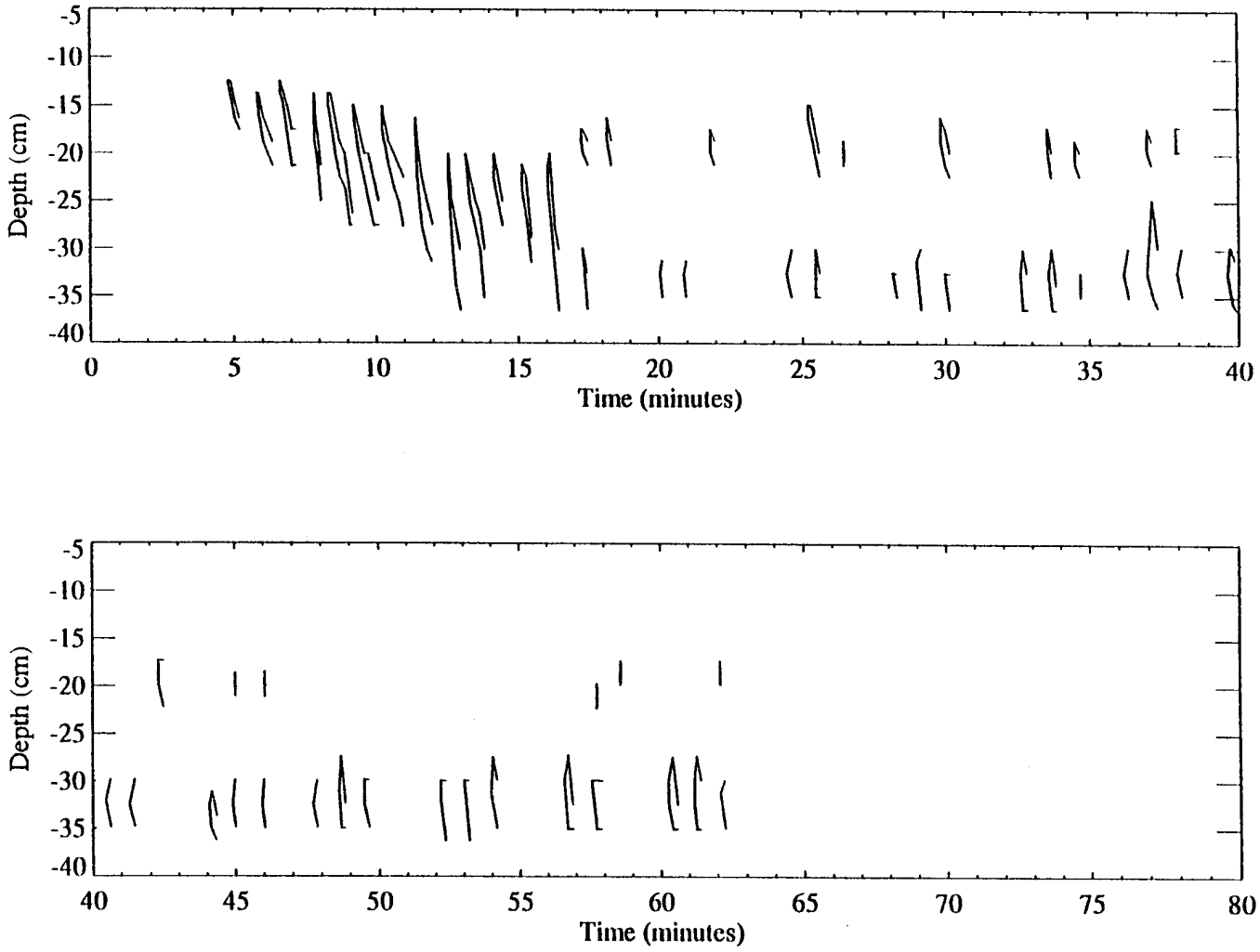

Figure 19. Observed regions of turbulence for Run 191 (a two-wave run with Wave 1 having a phase speed of 4.5 cm/sec and a peak-to-peak amplitude of 4.0 cm and Wave 2 having a phase speed of 3.5 cm/sec and a peak-to-peak amplitude of 2.0 cm).

Figure 18 shows, as expected, that the maximum and minimum floor excursions are larger and smaller, respectively, than the excursions for Run 171. The time-averaged amplitude over one beat period is 1.37 cm. Relative to the observed regions of turbulence for the previous run (Figure 17), the observed regions of turbulence for this run (Figure 19) show fewer mixing regions in the bottom of the tank at late times. Those mixing regions present are grouped into a series of two or three followed by a period of time where there is no activity. For example, Figure 19 shows internal mixing regions in the bottom of the tank at times of 41, 45, and 49 minutes, while there is no activity at 43 and 47 minutes. Looking at Figure 18 shows that the bottom floor has maximum excursions at 41, 45, and 49 minutes, corresponding to the times regions of turbulence are observed in the tank. The floor has minimum excursions at 43 and 47 minutes, corresponding to times no activity is observed.

The observed correlation of the bottom floor and the observed regions of activity is more noticeable in Run 191 than in Run 171 because of the larger differences between the maximum and minimum floor excursions. Thus, when the bottom floor excursions are large, a large amount of wave energy is transferred to the flow, and this energy results in mixing regions. When the floor excursions are small, a smaller amount of energy is transferred to the flow, and the flow remains stable.

Run 151 offers additional insight into this phenomenon. In this run, we used one wave with a phase speed of 4.5 cm/sec and a peak-to-peak amplitude of 3.0 cm and a second wave with a phase speed of 3.5 cm/sec and a peak-to-peak amplitude of 3.0 cm. Thus, both waves in this run have the same amplitude, but they have different phase speeds. The maximum wave amplitude for this run is identical to the maximum wave amplitude for Run 191.

The floor position vs. time and the observed regions of turbulence for Run 151 are shown in Figures 20 and 21, respectively. Figure 20 shows early K-H breaking and regular groupings of turbulence at later times. These groupings consist of two or three internal mixing regions in the bottom of the tank (two at early times and three at later times) and turbulence in the upper part of the tank at the same time. In between these grouping, there is no observed turbulence in the tank. These observations are consistent with what we observed in the other two-wave runs, and is consistent with the movement of the bottom floor (Figure 20).

Note in Figure 21 that the early wavebreaking (which appears to be K-H from the videos) takes on a slightly different form than we observed before (compare Figure 21 with the one-wave case of Run 161 shown in Figure 8b). In Figure 8b, the K-H overturning progresses monotonically from the top of the tank to the bottom of the tank ($t < \sim 16$ minutes). In Figure 21, this K-H overturning is greatly influenced by the motion of the bottom floor. Note, for example, around $t = 15$ minutes, which corresponds to a maximum excursion of the bottom floor, we only see turbulence in the middle part of the tank, and no turbulence in the lower part of the tank. In contrast, Figure 8b shows a regular progression of the K-H turbulence at this time.

The evolution of the mean flow for this run, averaged over one beat period, is shown in Figure 22. This mean flow evolution is similar to the one-wave case shown in Figure 9 in that a velocity ledge progresses downward toward the floor during the time K-H overturning is observed. Thereafter, the mean velocity is nearly constant with time. Note, however, that the mean velocity in the lower part of the tank is smaller in this case than in the one-wave case. This

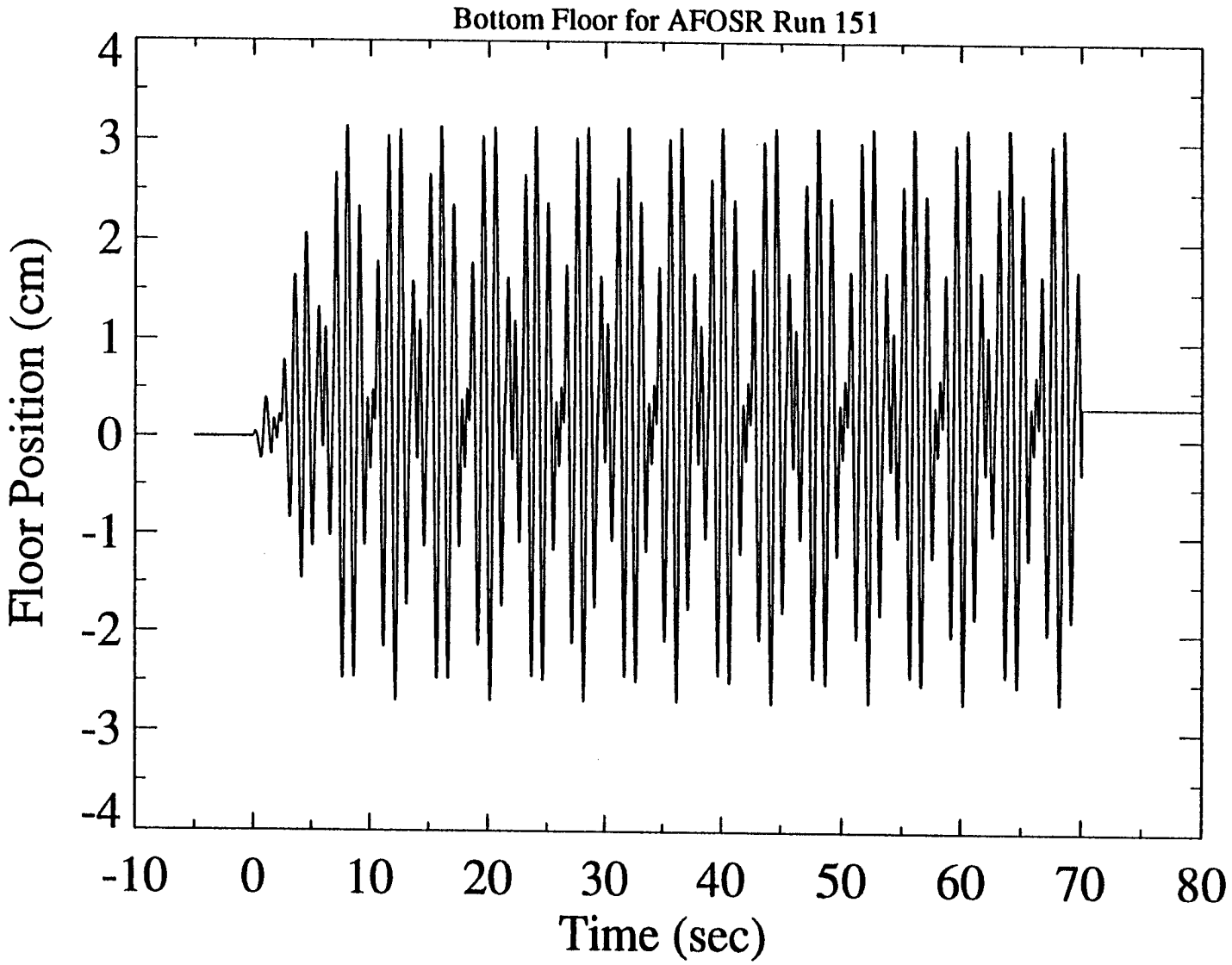

Figure 20. Floor position vs. time for Run 151 (a two-wave run with Wave 1 having a phase speed of 4.5 cm/sec and a peak-to-peak amplitude of 3.0 cm and Wave 2 having a phase speed of 3.5 cm/sec and a peak-to-peak amplitude of 3.0 cm).

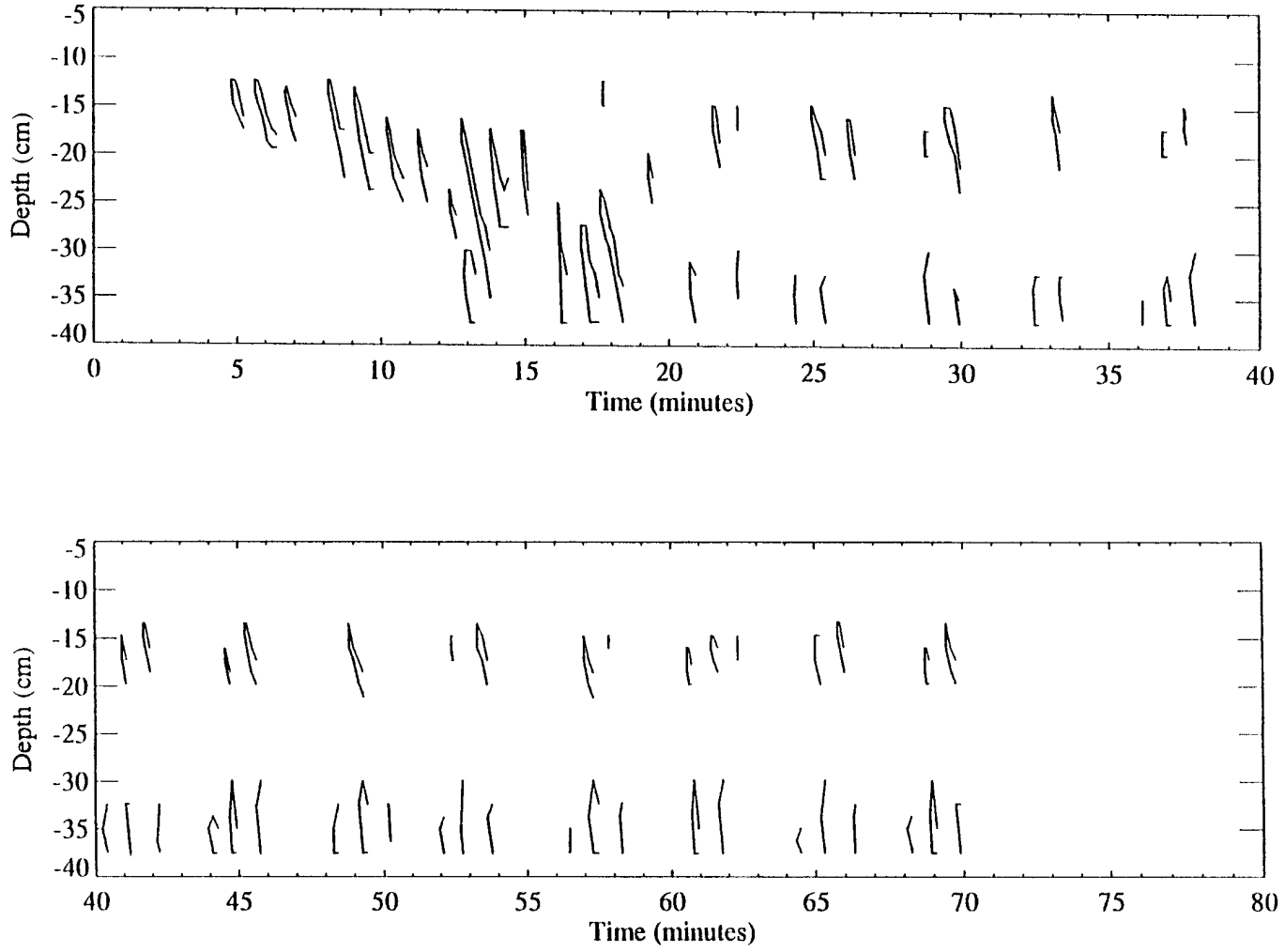

Figure 21. Observed regions of turbulence for Run 151 (a two-wave run with Wave 1 having a phase speed of 4.5 cm/sec and a peak-to-peak amplitude of 3.0 cm and Wave 2 having a phase speed of 3.5 cm/sec and a peak-to-peak amplitude of 3.0 cm).

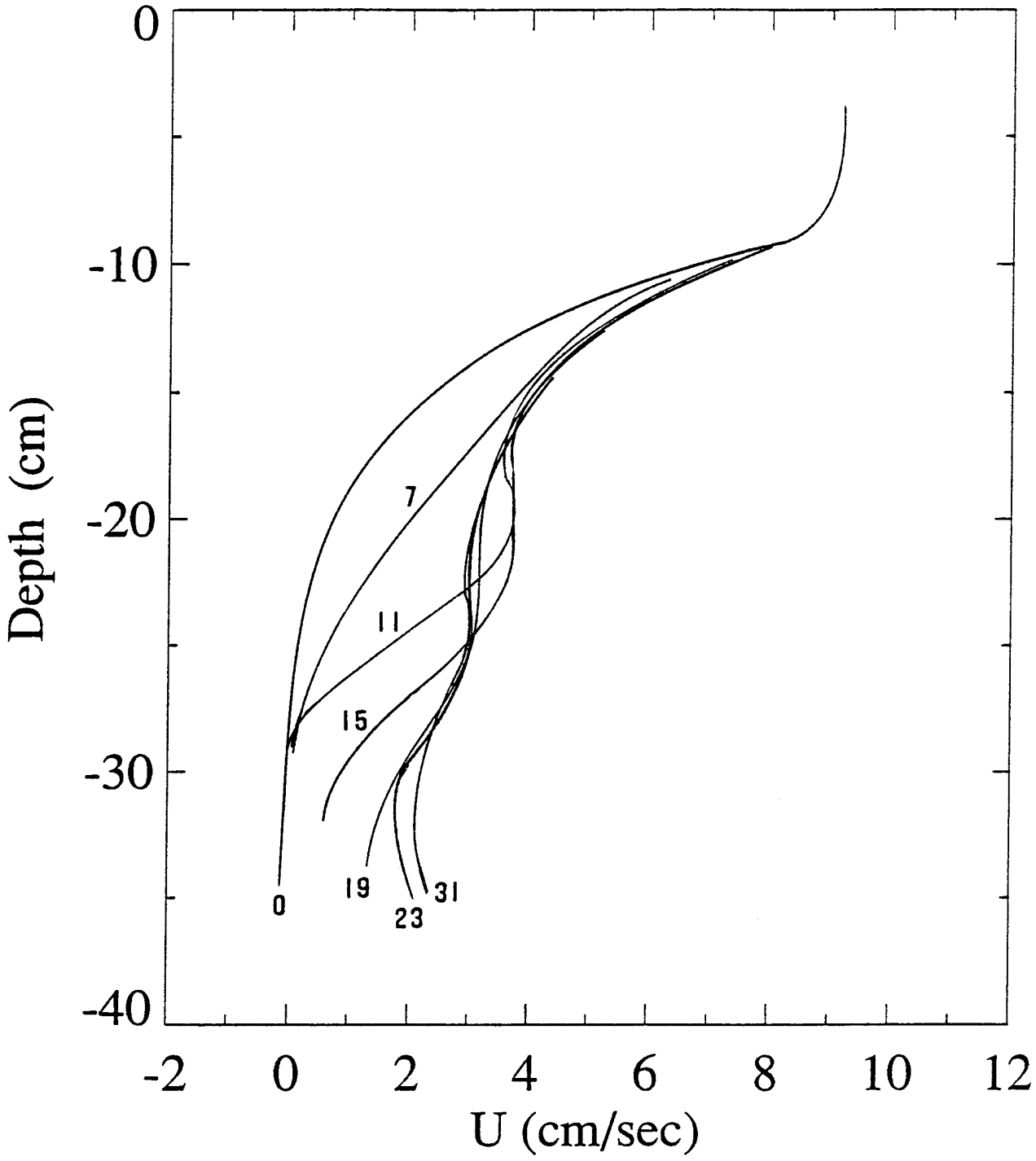

Figure 22. Evolution of the mean velocity profile with time in Run 151 (a two-wave run with Wave 1 having a phase speed of 4.5 cm/sec and a peak-to-peak amplitude of 3.0 cm and Wave 2 having a phase speed of 3.5 cm/sec and a peak-to-peak amplitude of 3.0 cm). Times are in minutes after the start of the bottom floor.

lower mean velocity allows more wave energy to be transferred to the upper part of the tank in this case, allowing more turbulence in the upper part of the tank at later times.

5. Summary and Comments

Gravity wave, critical wave interactions have been observed for both single-wave forcing and two-wave forcing. In the two-wave case, three different conditions have been presented. For both the single- and two-wave forcing, the initial overturning and turbulence appears to be Kelvin-Helmholtz in nature. This has been verified both with visual observations and with Richardson number contour plots. The mean velocity profiles exhibit a velocity ledge which moves downward, away from the critical layer and toward the bottom floor of the tank, with time. Later overturning appears to be a strong function of the bottom floor.

The importance of these results is the following:

a. These experiments are the first to quantify wavebreaking from gravity wave, critical layer interactions. This quantification has resulted in our characterizing the overturning as due to Kelvin-Helmholtz instabilities rather than due to convective overturning. K-H wavebreaking was speculated by us earlier (Delisi and Dunkerton, 1989), but there was no previous quantitative data to substantiate that hypothesis.

b. This is the first laboratory experiment of which we are aware in which a stable mean flow is perturbed by an internal gravity wave to create a flow which is unstable to Kelvin-Helmholtz instabilities. The minimum Richardson number in the mean flow, at depths where K-H instabilities are later observed, can be 20 or higher. When the wave shear is added to this mean flow shear, the Richardson number falls below one-quarter, allowing Kelvin-Helmholtz instabilities to develop.

c. These experiments have shown that gravity wave, critical layer interactions can be studied in the laboratory and that quantitative measurements of those interactions can be obtained. We believe the feasibility of future studies, involving compact wave sources (which are relevant to atmospheric flows), has been shown and should be pursued at a later date.

REFERENCES

Andrews, D.G., J.R. Holton, and C.B. Leovy, 1987: *Middle Atmosphere Dynamics*. Academic Press, New York.

Benney, D.J., and R.F. Bergeron, 1969: A New Class of Nonlinear Waves in Parallel Flows. *Stud. Appl. Math., 48*, 181-204.

Booker, J.R., and F.P. Bretherton, 1967: The Critical Layer for Internal Gravity Waves in a Shear Flow. *J. Fluid Mech., 27*, 513-539.

Bretherton, F.P., 1966: The Propagation of Internal Gravity Waves in a Shear Flow. *Quart. J. Roy. Meteor. Soc., 92*, 446-880.

Bretherton, F.P., P. Hazel, S.A. Thorpe, and I.R. Wood, 1967: Appendix to the paper by P. Hazel, The Effect of Viscosity and Heat Conduction on Internal Gravity Waves at a Critical Level. *J. Fluid Mech., 30*, 775-783, (Appendix on pp. 781-783).

Brown, S.N., and K. Stewartson, 1980: On the Nonlinear Reflextion of a Gravity Wave at a Critical Level. Part 1. *J. Fluid Mech., 100*, 557-595.

Delisi, D.P., and G. Corcos, 1973: A Study of Internal Waves in a Wind Tunnel. *Boundary-Layer Meteorol., 5*, 121-137.

Delisi, D.P., 1988: *Studies of Internal Wave/Mean Flow Interactions*. Northwest Research Associates Report NWRA-CR-88-R029, Bellevue, WA.

Delisi, D.P., and T.J. Dunkerton, 1989: Laboratory Observations of Gravity Wave Critical-Layer Flows. *Pure and Appl. Geophys., 130*, 445-661.

Delisi, D.P., and T.J. Dunkerton, 1994: Laboratory Observations of Gravity Wave, Critical Layer Flows Using Single and Double Wave Forcing. *Appl. Mech. Rev., 47*, No. 6, Part 2, 113-117.

Dunkerton, T.J., 1980: A Lagrangian Mean Theory of Wave, Mean-flow Interaction with Applications to Nonacceleration and its Breakdown. *Rev. Geophys. Space Phys., 18*, 387-400.

Dunkerton, T.J. 1981: Wave Transcience in a Compressible Atmosphere, Part I: Transient Internal Wave, Mean-Flow Interaction. *J. Atmos. Sci., 38*, 281-297.

Dunkerton, T.J., 1982: Wave Transience in a Compressible Atmosphere, Part 3: The Saturation of Internal Gravity Waves in the Mesosphere. *J. Atmos. Sci., 39*, 1042-1051.

Dunkerton, T.J., and D.C. Fritts, 1984: The Transient Gravity Wave Critical Layer, Part 1: Convective Adjustment and the Mean Zonal Acceleration. *J. Atmos. Sci., 41*, 992-1007.

Dunkerton, T.J., and R.E. Robins, 1992: Radiating and Nonradiating Modes of Secondary Instability in a Gravity-Wave Critical Layer. *J. Atmos. Sci., 49*, 2546-2559.

Fritts, D.C., 1978: The Nonlinear Gravity Wave-Critical Level Interaction. *J. Atmos. Sci., 35*, 397-413.

Fritts, D.C., 1979: The Excitation of Radiating Waves and Kelvin-Helmholtz Instabilities by the Gravity Wave-Critical Layer Interaction. *J. Atmos. Sci., 36*, 12-23.

Fritts, D.C., 1982: The Transient Critical-Level Interaction in a Boussinesq Fluid. *J. Geophys. Res., 87*, 7997-8016.

Fritts, D.C., 1984: Gravity Wave Saturation in the Middle Atmosphere: A Review of Theory and Observations. *Rev. Geophys. Space Phys., 22*, 275-308.

Grimshaw, R., 1975: Nonlinear Internal Gravity Waves and Their Interaction with the Mean Wind. *J. Atmos. Sci., 32*, 1779-1793.

Koop, C.G., 1981: A Preliminary Investigation of the Interaction of Internal Gravity Waves With a Steady Shearing Motion. *J. Fluid Mech., 113*, 347-386.

Koop, C.G. and B. McGee, 1986: Measurements of Internal Gravity Waves in a Continuously Stratified Shear Flow. *J. Fluid Mech., 172*, 453-480.

Lindzen, R.S., 1981: Turbulence and Stress Owing to Gravity Wave and Tidal Breakdown. *J. Geophys. Res., 86*, 9707-9714.

Maslowe, S.A., 1973: Finite-Amplitude Kelvin-Helmholtz Billows. *Bound-Layer Meteor., 5*, 43-52.

Maslowe, S.A., 1977: Weakly Nonlinear Stability Theory of Stratified Shear Flows. *Quart. J. Roy. Meteor. Soc., 103*, 769-783.

Maslowe, S.A., 1986: Critical Layers in Shear Flows. *Ann. Rev. Fluid Mech., 18*, 405-432.

Miles, J.W., 1961: On Stability of Heterogeneous Shear Flows. *Internal Fluids Mech., 10.*

Nastrom, G.D., D.C. Fritts, and K.S. Gage, 1987: An Investigation of Terrain Effects on the Mesoscale Spectrum of Atmospheric Motions. *J. Atmos. Sci., 44*, 3087-3096.

Orlanski, I., and K. Bryan, 1969: Formation of the Thermocline Step Structure by Large-Amplitude Internal Gravity Waves. *J Geophys. Res., 74*, 6975-6983.

Plumb, R.A., and A.D. McEwan, 1978: The Instability of a Forced Standing Wave in a Viscous Stratified Fluid: A Laboratory Analogue of the Quasi-Biennial Oscillation. *J. Atmos. Sci., 35*, 1827-1839.

Thorpe, S.A., 1968: A Method of Producing a Shear Flow in a Stratified Fluid. *J. Fluid Mech., 32*, 693-704.

Thorpe, S.A., 1973: Turbulence in Stably Stratified Fluids: A Review of Laboratory Experiments. *Boundary-Layer Meteorol., 5*, 95-119.

Thorpe, S.A., 1981: An Experimental Study of Critical Layers. *J. Fluid Mech., 103*, 321-344.

Willert, C.E., and M. Gharib, 1991: Digital Particle Image Velocimetry. *Experiments in Fluids, 10*, 181.

APPENDIX

Reprint of

"Laboratory Observations of Gravity Wave, Critical Layer

Flows Using Single and Double Wave Forcing"

by

Donald P. Delisi
and
Timothy J. Dunkerton

Applied Mechanics Review
Vol 47, 1994

Laboratory observations of gravity wave, critical layer flows using single and double wave forcing

Donald P Delisi and Timothy J Dunkerton

Northwest Research Associates, PO Box 3027, Bellevue WA 98009-3027

part of "Mechanics USA 1994" edited by AS Kobayashi
Appl Mech Rev vol 47, no 6, part 2, June 1994

ASME Reprint No AMR146

Laboratory observations of gravity wave, critical layer flows using single and double wave forcing

Donald P Delisi and Timothy J Dunkerton

Northwest Research Associates, PO Box 3027, Bellevue WA 98009-3027

Laboratory measurements of gravity wave, critical layer flows are presented. The measurements are obtained in a salt-stratified annular tank, with a vertical shear profile. Internal gravity waves are generated at the floor of the tank and propagate vertically upward into the fluid. At a depth where the phase speed of the wave equals the mean flow speed, defined as a critical level, the waves break down, under the right forcing conditions, generating small scale turbulence. Two cases are presented. In the first case, the wave forcing is a single, monochromatic wave. In this case, the early wave breaking is characterized as Kelvin-Helmholtz breaking at depths below the critical level. Later wave breaking is characterized by weak overturning in the upper part of the tank and regular, internal mixing regions in the lower part of the tank. In the second case, the wave forcing is two monochromatic waves, each propagating with a different phase speed. In this case, the early wave breaking is again Kelvin-Helmholtz in nature, but later wave breaking is characterized by sustained overturning in the upper part of the tank with internal mixing regions in the lower part of the tank. Mean velocity profiles are obtained both before and during the experiments.

CONTENTS

INTRODUCTION

Gravity waves occur naturally in the atmosphere and are important in atmospheric circulation for transporting momentum and for generating turbulence, thereby producing mixing. One mechanism for the breakdown of gravity waves into turbulence occurs in a shear flow when the wave approaches its critical level, which is defined as the level where the horizontal phase speed of the wave equals the mean flow speed (Booker and Bretherton, 1967). When this occurs, the wave's vertical propagation is modified, wave energy is transferred to the mean flow, and turbulence can be generated.

To predict atmospheric circulation, it is important to understand how gravity waves propagate and break down. Our lack of understanding of the interactions between large-scale waves and small-scale turbulence and mixing is one of the factors that limits our ability to predict atmospheric conditions very far in advance.

The bulk of our present understanding of gravity wave, critical level interactions has come from theoretical and numerical studies (see e.g., Bretherton, 1966; Lindzen, 1981; Fritts, 1984; Maslowe, 1986; and Dunkerton and Robins, 1992, to name a few). In addition, there have been attempts at observational studies of this phenomenon (e.g., Merrill and Grant, 1979).

In the laboratory, studies of gravity wave, critical level interactions under controlled conditions have been reported by Bretherton et al., 1967; Thorpe, 1973; Koop, 1981; Koop and McGee, 1986; and Delisi and Dunkerton, 1989. In these experiments, the reported results have typically been qualitative in nature, and most experiments were limited by the physical dimensions of the test facility, which limited the duration of the interactions.

EXPERIMENTAL FACILITY

The experimental facility used in these experiments is described in detail in Delisi and Dunkerton (1989). Our facility is a modification of a laboratory wave tank developed by Plumb and McEwan (1978). A schematic of the facility is given in Figure 1. The tank is annular, with an outer diameter of 1.8 m, an inner diameter of 1.2 m, and a depth

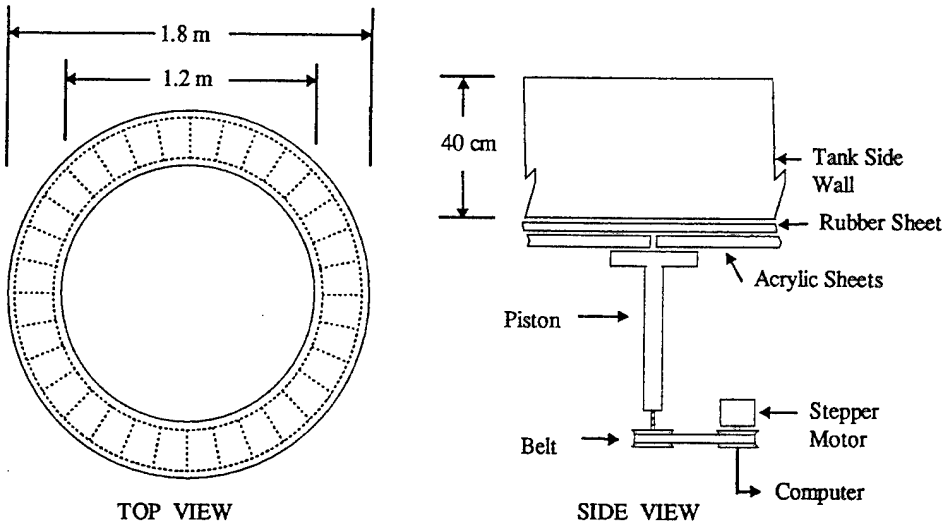

FIG 1. Schematic drawing of the experimental facility. One of 32 piston assemblies is shown in the side view

of 40 cm. The bottom of the tank is a rubber sheet overlaying individual acrylic sheets. The common boundaries of each pair of acrylic sheets rest on top of a vertical piston which is driven by a stepper motor. A computer controls the movement of each stepper motor, driving each section of the bottom floor of the tank vertically. In this way, we can prescribe the motion of the bottom floor as a wave which propagates around the bottom of the tank with a known amplitude, wavelength, and phase speed. In this series of experiments, the computer controlled the floor to move as either a single, monochromatic wave or as two monochromatic waves, with different phase speeds. We used wavenumber two in all the experiments.

To perform an experiment, we fill the tank with a stratified salt water solution, rotate a floating lid on the water surface to create a vertical shear profile, then propagate one or two waves on the bottom floor of the tank by moving the floor vertically with the stepper motors. Measurements consist of instantaneous density data from an oscillating conductivity probe, bottom floor position data, mean and instantaneous velocity profiles from streak photographs of neutrally buoyant particles, and 35-mm and video pictures of shadowgraph flow visualization which show the turbulent regions.

The initial velocity profile before the two-wave run is shown in Figure 2. This profile shows a nearly constant velocity in the upper layer, where the lid has mixed the fluid, and a nearly exponential velocity profile beneath the mixed region.

We used two, linearly stratified density layers in these experiments. The uppermost layer is a highly stratified region whose purpose is to minimize the depth of the mixed layer generated by the rotating lid. The initial density profile for the two-wave experiment is shown in Figure 3. The Brunt-Vaisala frequency, N, for the top layer is 1.62 sec^{-1}, and N for the bottom layer is 1.02 sec^{-1}, where $N = (g/\rho\, d\rho/dz)^{1/2}$, where g is the acceleration due to gravity, ρ is density, and z is the vertical coordinate.

RESULTS

One wave results

In this experiment, we forced the bottom with a single wave with a peak-to-peak amplitude of 4.0 cm and a phase speed of 4.5 cm/sec. The movement of the bottom floor was not exactly sinusoidal, but was asymmetric to match the propagating wavefronts in a nonsheared, linearly stratified fluid. This asymmetry in the forcing function is intended to mimic the generated gravity wave and to, therefore, reduce the higher harmonics that would be generated by using a sinusoidal wave on the bottom floor.

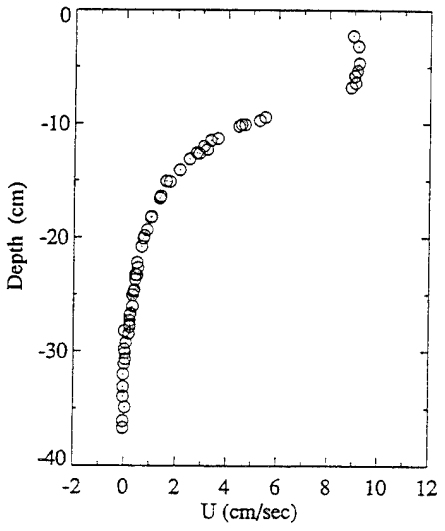

FIG 2. The initial velocity profile before a two-wave experiment.

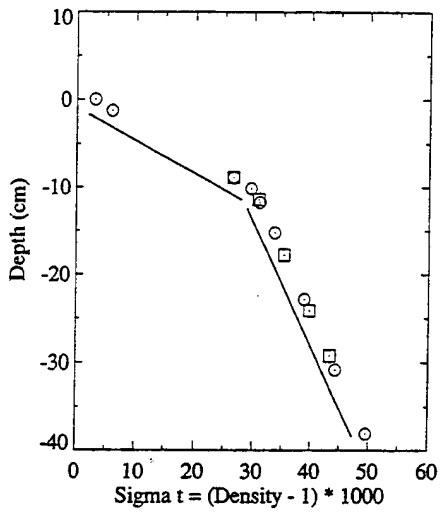

FIG 3. The initial density profile before a two-wave experiment. Circles are observations taken during the filling of the tank; squares are probe samples taken after filling the tank. Straight lines are drawn for comparison to linearity.

Videotapes of shadowgraph visualization clearly show regions of overturning and turbulence as a function of time. We have analyzed these videotapes to determine the vertical extent of the breaking regions as a function of time. Figure 4 shows the observed regions of turbulence vs time after the start of the bottom floor. Note in Figure 4 that the overturning first appears near the top of the tank and progresses downwards, toward the bottom floor, from t = 0 to t ~ 13 min. From observations of the videos, this overturning appears to be Kelvin-Helmholtz (K-H) in nature. For t > ~13 min, most of the observed turbulence occurs in mixing regions in the bottom half of the tank (Delisi and Dunkerton, 1989), with only sporadic, patchy turbulence being observed in the top half of the tank. The evolution of the mean velocity profile is shown in Figure 5, and shows that the initial mean velocity profile is modified by a velocity ledge which progresses downwards with time. These mean flow modifications are qualitatively similar to those predicted by numerical simulations (Dunkerton and Robins, 1992), although the overturning regions in those simulations are characterized as convective overturning rather than K-H. In our laboratory experiments, the initial K-H overturning is observed during the time the ledge is a feature in the mean flow; the mixing regions appear to occur when the velocity in the lower part of the tank is more nearly constant.

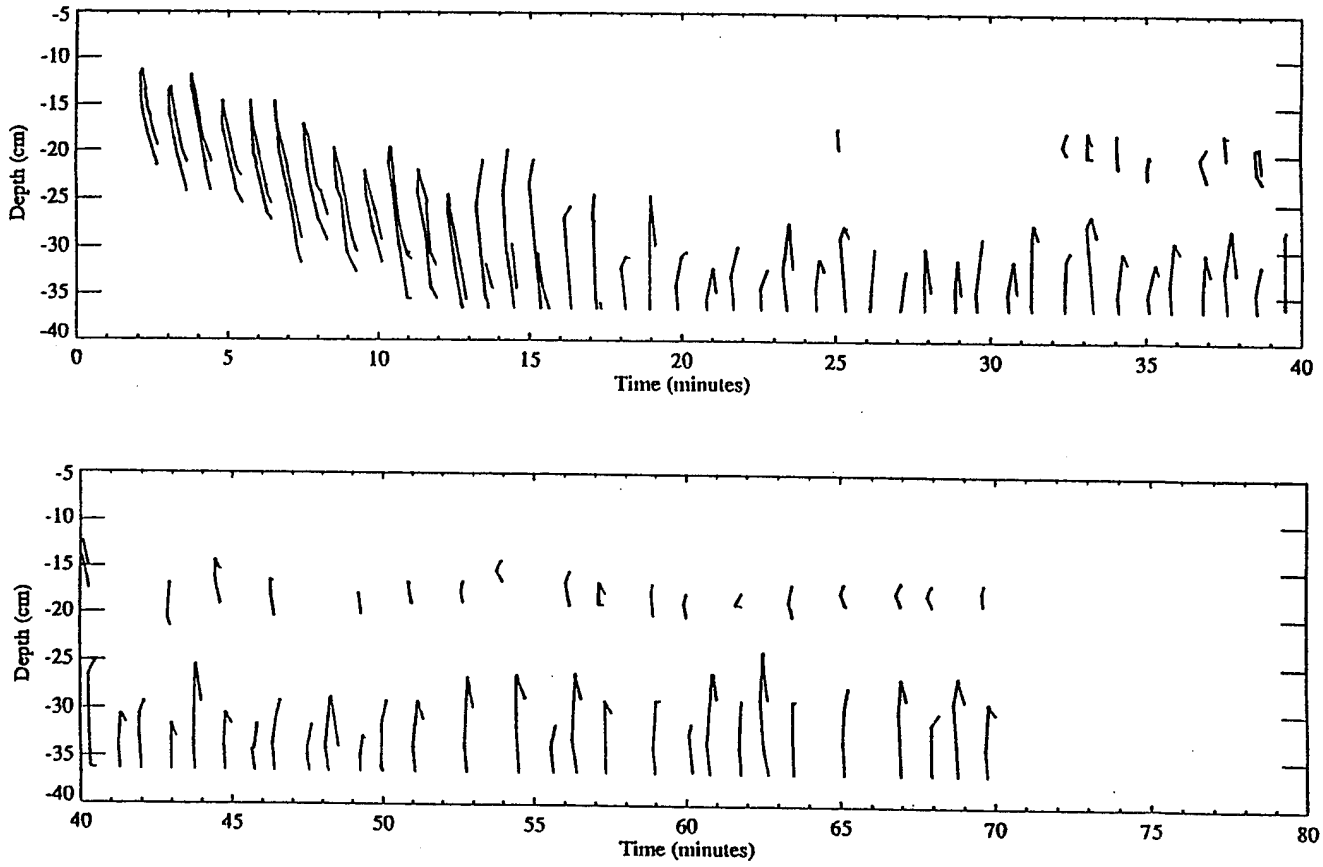

FIG 4. Observed regions of turbulence in a one-wave experiment. Time is minutes after the start of the experiment.

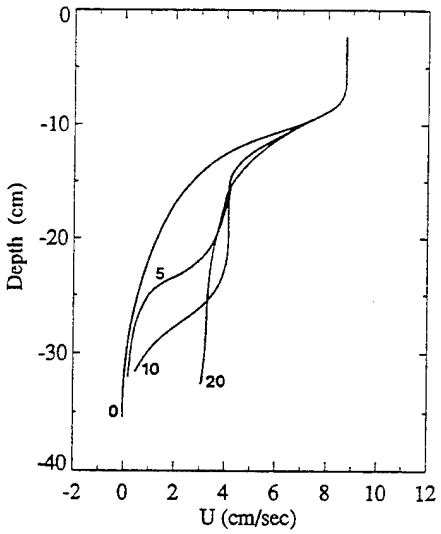

FIG 5. Mean flow velocity profiles for a one-wave experiment. The mean flow is the average over one wave cycle. Time is minutes after the start of the experiment.

Two wave results

In this experiment, we forced the bottom with two waves. Each wave had a peak-to-peak amplitude of 3.0 cm. One wave had a phase speed of 4.5 cm/sec, and the second wave had a phase speed of. 3.5 cm/sec. With these choices, the bottom forcing has a beat period of 4 minutes.

The overturning regions for this case are shown in Figure 6. For early time, $t < \sim 13$ min, the shadowgraph visualizations show that the breaking regions are K-H, as in the one-wave case. Figure 6 also shows an early pattern of breaking similar to the pattern shown for the one-wave case in that the breaking regions occur initially high in the tank and progress towards the floor of the tank with time. (The lack of wave breaking before $t \sim 5$ min is probably attributable to a ramping up of wave amplitude in this run vs the one-wave case where the waves started at full amplitude at $t = 0$).

At $t > \sim 13$ min, the shadowgraph visualization shows a significant difference between the one-wave and the two-wave cases. In the one-wave case, the internal mixing region which occurs near the bottom of the tank appears once every wave cycle. Only small, sporadic regions of turbulence appear above these regions, at depths around 15 cm.

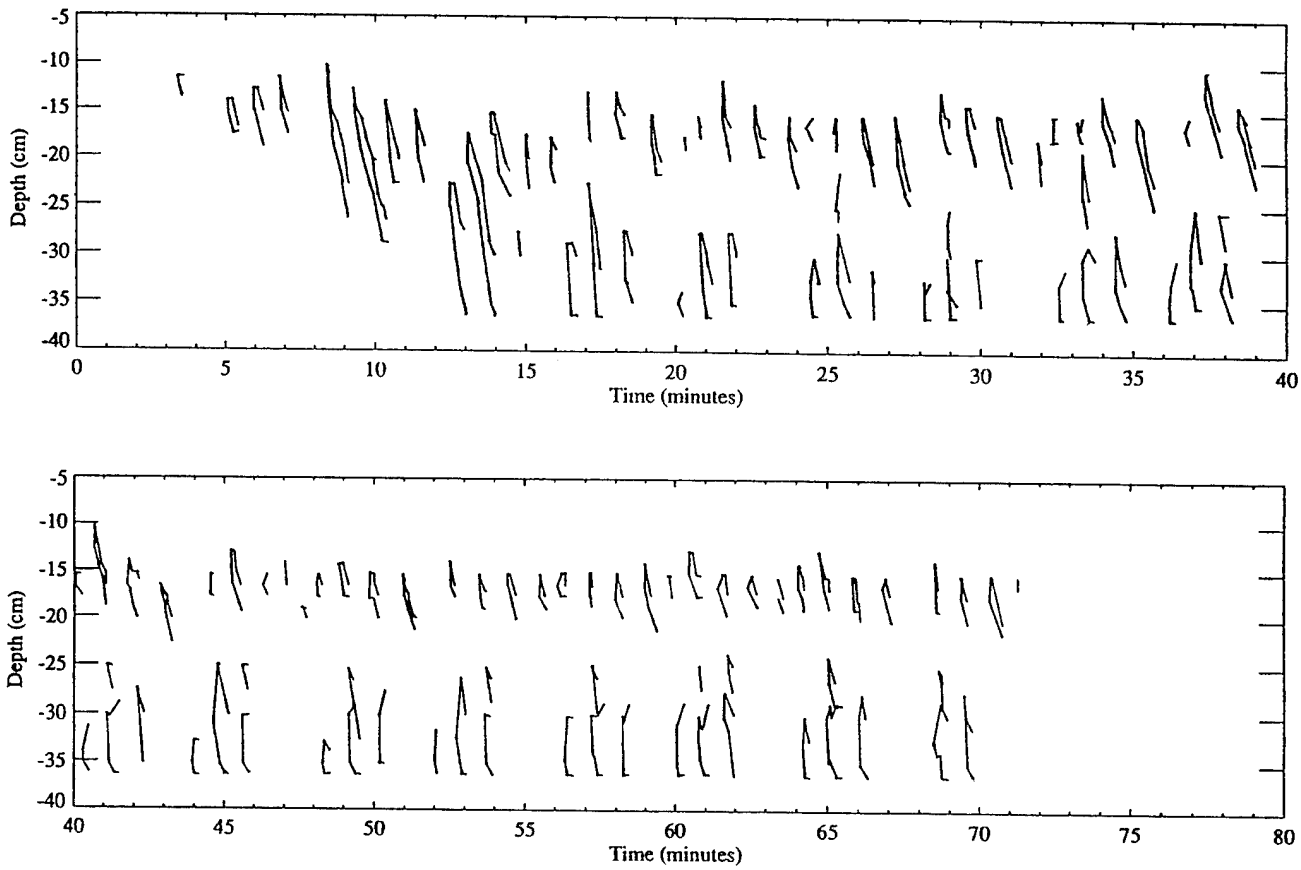

FIG 6. Observed regions of turbulence in a two-wave experiment. Time is minutes after the start of the experiment.

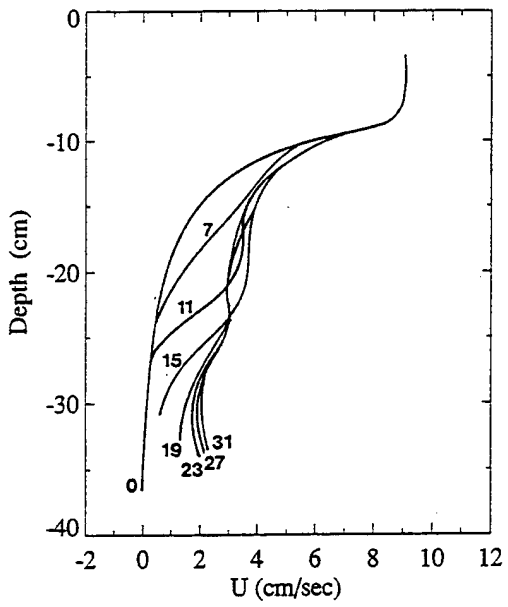

FIG 7. Mean flow velocity profiles for a two-wave experiment. The mean flow is the average over one beat period. Time is minutes after the start of the experiment.

In the two-wave case, around t ~ 13 min, the turbulent regions appear to bifurcate, with K-H overturning appearing at a depth around 17 cm and a mixing region, similar to that in the one-wave case, appearing in the lower portion of the tank. The K-H regions in the upper part of the tank appear more or less periodically. This is in contrast to the turbulent regions in the bottom of the tank, which appear in packets of three. The time interval between these packets is due to the beating of the two bottom waves, which, as in the one-wave case, are asymmetric.

The evolution of the mean flow, averaged over one beat period, for the two-wave case is shown in Figure 7. This mean flow evolution is similar to the one-wave case in that a velocity ledge progresses downward toward the floor during the time K-H overturning is observed. Thereafter, the mean velocity is nearly constant with time.

SUMMARY

Gravity wave, critical layer observations for both single wave forcing and two-wave forcing have been presented. For both cases, the initial overturning appears to be Kelvin-Helmholtz in nature, and the mean velocity profiles exhibit a velocity ledge which progresses downward toward the floor with time. Later overturning appears quite different in the two cases, with prolonged K-H overturning in the upper regions of the tank in the two-wave case.

ACKNOWLEDGEMENT

The authors thank Lee E. Piper for his assistance in performing the experiments and Wilbur F. Pierce IV for assistance in analyzing the data. This study was supported by the Air Force Office of Scientific Research under contracts F49620-92-C-0005 and F49620-92-C-0033.

REFERENCES

Booker JR and Bretherton FP (1967), The critical layer for internal gravity waves in a shear flow, *J Fluid Mech 27*, 513-539.

Bretherton FP (1966), The propagation of internal gravity waves in a shear flow, *Quart J Roy Meteor Soc 92*, 446-480.

Bretherton FP, Hazel P, Thorpe SA, and Wood IR (1967), Appendix to the paper by Hazel P, The effect of viscosity and heat conduction on internal gravity waves at a critical level, *J Fluid Mech 30*, 775-783, (Appendix on pp. 781-783).

Delisi DP and Dunkerton TJ (1989), Laboratory observations of gravity wave critical-layer flows, *Pure and Appl Geophys 130*, 445-461.

Dunkerton TJ and Robins RE (1992), Radiating and nonradiating modes of secondary instability in a gravity-wave critical layer, *J Atmos Sci 49*, 2546-2559.

Fritts DC (1984), Gravity wave saturation in the middle atmosphere: a review of theory and observations, *Rev Geophys and Space Phys 22*, 275-308.

Koop CG (1981), A preliminary investigation of the interaction of internal gravity waves with a steady shearing motion, *J Fluid Mech 113*, 347-386.

Koop CG and McGee B (1986), Measurements of internal gravity waves in a continuously stratified shear flow, *J Fluid Mech 172*, 453-480.

Lindzen RS (1981), Turbulence and stress due to gravity wave and tidal breakdown, *J Geophys Res 86C*, 9707-9714.

Maslowe SA (1986), Critical layers in shear flows, *Ann Rev Fluid Mech 18*, 405-432.

Merrill JT and Grant JR (1979), A gravity wave-critical level encounter observed in the atmosphere, *J Geophys Res 84*, 6315-6320.

Plumb RA and McEwan AD (1978), The instability of a forced standing wave in a viscous stratified fluid: a laboratory analogue of the quasi-biennial oscillation, *J Atmos Sci 35*, 1827-1839.

Thorpe SA (1973), Turbulence in stably stratified fluids: a review of laboratory experiments, *Boundary-Layer Meteorol 5*, 95-119.